

1 **Processing and performance of topobathymetric LiDAR**
2 **data for geomorphometric and morphological**
3 **classification in a high-energy tidal environment in the**
4 **coastal zone**

5
6 **M.S. Andersen¹, Á. Gergely¹, Z. Al-Hamdani², F. Steinbacher³, L.R. Larsen⁴,**
7 **V.B. Ernstsén¹**

8 [1] Department of Geosciences and Natural Resource Management, University of
9 Copenhagen, Denmark

10 [2] Geological Survey of Denmark and Greenland, Denmark

11 [3] Airborne Hydro Mapping GmbH, Austria

12 [4] NIRAS, Denmark

13 Correspondence to: V. B. Ernstsén (vbe@ign.ku.dk)

14
15 **Abstract**

16 The transition zone between land and water is difficult to map with conventional
17 geophysical systems due to shallow water depth and often harsh environmental
18 conditions. The emerging technology of airborne topobathymetric Light Detection And
19 Ranging (LiDAR) is capable of providing both topographic and bathymetric elevation
20 information, using only a single green laser, resulting in a seamless coverage of the
21 land-water transition zone. However, there is no transparent and reproducible method
22 for processing green topobathymetric LiDAR data into a Digital Elevation Model
23 (DEM). The general processing steps involve data filtering, water surface detection and
24 refraction correction. Specifically, the procedure of water surface detection, solely using
25 green laser LiDAR data, has not previously been described in detail. The aim of this
26 study was to fill this gap of knowledge by developing a step-by-step procedure for
27 modelling the water surface using the green laser LiDAR data. The detailed description
28 of the processing method augments its reliability, makes it user friendly and repeatable.

1 A DEM was obtained from the processed topobathymetric LiDAR data collected in
2 spring 2014 from the Knudedyb tidal inlet system in the Danish Wadden Sea. The
3 vertical accuracy of the LiDAR data is determined to ± 8 cm at a 95% confidence level,
4 and the horizontal accuracy is determined as the mean error to ± 10 cm. The LiDAR
5 technique is found capable of detecting features with a size of less than 1 m^2 . The
6 derived high resolution DEM was applied for detection and classification of
7 geomorphometric and morphological features in the study area. Initially, stage (or
8 elevation in relation to tidal range) was used to divide the area of investigation into the
9 different tidal zones, i.e. subtidal, intertidal and supratidal. Subsequently, a combination
10 of statistical neighbourhood analyses (Bathymetric Positioning Index, moving average
11 and standard deviation) with varying window sizes, combined with the first derivative
12 slope and the area/perimeter-ratio were used to identify and characterise morphometric
13 units. Finally, these morphometric units were classified into six different types of
14 morphological features (i.e. subtidal channel, intertidal flat, intertidal creek, linear bar,
15 swash bar and beach dune). The developed classification method is adapted and applied
16 to a specific case, but it can be transferred to other cases and environments.

17

18 **1 Introduction**

19 The coastal zone is under pressure from human exploitation in many and various ways.
20 Many large cities are located near the coast, and they grow gradually with the increase
21 in worldwide population and urbanization. Many industrial activities take place in close
22 vicinity to the coast, e.g. fishery, construction, maintenance dredging for safety of
23 navigation, and mining for raw materials. The coastal zone also provides the setting for
24 many recreational and touristic activities, such as sailing, swimming, hiking, diving and
25 surfing. In addition to human exploitation, climate change also poses a future threat
26 with a predicted rising sea level and increasing storm intensity and frequency, expected
27 to cause erosion and flooding in the coastal zone (Mousavi et al., 2011). All these
28 pressures and different interests underpin the societal need for high resolution mapping,
29 monitoring, and sustainably managing of the coastal zone.

30 The transition zones between land and water have been difficult or even impossible to
31 map and investigate in high spatial resolution due to the challenging environmental

1 conditions. The airborne near-infrared (NIR) Light Detection and Ranging (LiDAR) is a
2 technique often used for measuring high-resolution topography, however, NIR laser is
3 incapable of measuring bathymetry due to the absorption and reflection of the laser light
4 at the water surface. Traditionally, high-resolution bathymetry is measured with a
5 multibeam echosounder (MBES) system mounted on a vessel, but it does not cover the
6 bathymetry in the shallow water due to the vessel draft limitation.

7 NIR LiDAR and MBES are applied in different environments; however, the data are
8 very similar and the processed high-resolution topography/bathymetry are both often
9 captured in a Digital Elevation Model (DEM). The processed DEM may be applied for
10 various purposes, e.g. for geomorphological mapping. Previous studies classifying
11 morphology in either terrestrial or marine environments have been performed numerous
12 times (Al-Hamdani et al., 2008; Cavalli and Marchi, 2008; Höfle and Rutzinger, 2011;
13 Ismail et al., 2015; Kaskela et al., 2012; Lecours et al., 2016; Sacchetti et al., 2011).
14 These classification studies generally focus on either the marine or the terrestrial
15 environment, and they do not cover the small-scale morphology in the shallow water at
16 the land-water transition zones, due to the challenges of collecting data in these high-
17 energy environments. A new generation of airborne green topobathymetric LiDAR
18 enables high resolution measurements of both topography and shallow bathymetry, and
19 for that reason it is specifically suited to map the land-water transition zone (Guenther,
20 1985; Jensen, 2009; Pe'eri and Long, 2011). The potential of merging morphological
21 classifications of marine and terrestrial environments enables a holistic approach for
22 managing the coastal zone.

23 Topobathymetric LiDAR is based on continuous measurements of the distance between
24 an airplane and the ground/seabed. The distance (or range) is calculated by half the
25 travel time of a laser beam, going from the airplane to the surface of the earth and back
26 to the airplane. The wavelength of the laser beam is in the green spectrum, usually 532
27 nm, since this wavelength is found to attenuate the least in the water column, resulting
28 in the largest penetration depth of the laser (Jensen, 2009). In literature, topobathymetric
29 LiDAR data is sometimes referred to as either bathymetric LiDAR or Airborne LiDAR
30 bathymetry (ALB). These are just different terms with the same meaning, and in this
31 paper, topobathymetric LiDAR is preferred, since it describes the system's ability to
32 simultaneously measure bathymetry as well as topography.

1 A single laser beam may encounter many targets of varying nature on its way from the
2 airplane and back again, and different processes are influencing the laser beam
3 propagation through air and water. First, the laser beam may be reflected by targets in
4 the air, such as birds or dust particles, and these can show up as LiDAR reflection points
5 in the space between the airplane and the surface. When encountering water, the speed
6 of the laser decreases from $3 \times 10^8 \text{ ms}^{-1}$ to e.g. $2.25 \times 10^8 \text{ ms}^{-1}$ in 10°C freshwater or
7 e.g. $2.24 \times 10^8 \text{ ms}^{-1}$ in 10°C saltwater of 30 PSU (Millard and Seaver, 1990).

8 The changing speed of the laser beam also affects the direction of the laser beam when
9 penetrating the water surface with an angle different from nadir (Fig. 1) (Guenther,
10 2007; Jensen, 2009). The laser beam will be refracted according to Snell's Law
11 (Mandlbürger et al., 2013):

$$12 \frac{\sin \alpha_{\text{air}}}{\sin \alpha_{\text{water}}} = \frac{c_{\text{air}}}{c_{\text{water}}} = \frac{n_{\text{water}}}{n_{\text{air}}} \quad (1)$$

13 where α_{air} is the incidence angle of the laser beam relative to the normal vector of the
14 water surface and α_{water} is the refraction angle in water. n_{water} and n_{air} are the
15 refractive indices of water and air, respectively (Mandlbürger et al., 2013).

16 The penetration depth in water is limited by the attenuation of the laser beam. Water
17 molecules, suspended sediment and dissolved material all act on the laser beam by
18 absorption and scattering, resulting in substantial reduction in power as the signal
19 propagates into the water (Guenther, 2007; Mandlbürger et al., 2013; Steinbacher et al.,
20 2012). The laser beam also diverges in the water column, resulting in a wider laser
21 beam footprint (Guenther et al., 2000), and this effect reduces the resolving capability of
22 fine-scale morphology the deeper the laser beam penetrates.

23 The returned signal is represented as a distribution of energy over time, also called the
24 'full-waveform' (Alexander, 2010; Chauve et al., 2007; Mallet and Bretar, 2009). The
25 peaks in the full-waveform are detected as individual targets encountered by the
26 propagating laser beam. If the laser hits two targets with a small vertical difference,
27 such as a water surface and seabed in very shallow water, then the two peaks in the full-
28 waveform may merge together, resulting in the detection of only one target (Fig. 1).
29 This results in a detection minimum of successive returns from a single laser pulse, and
30 the vertical distance within this minimum is referred to as the 'dead zone' (Mandlbürger

1 et al., 2011; Nayegandhi et al., 2009). The dead zone is a clear limitation to the LiDAR
2 measurements, which is an important parameter to consider in very shallow water, such
3 as intertidal environments.

4 The raw LiDAR measurements are spatially visualized as a point cloud, with each point
5 representing an individual target. The point cloud must be piped through a series of
6 steps before it can take shape as a DEM. Most of the processing steps required to
7 process raw topobathymetric LiDAR data to a DEM are similar to the processing steps
8 of topographic LiDAR data (Huising and Gomes Pereira, 1998). However, additional
9 processing steps are required for topobathymetric LiDAR data due to the refraction of
10 the laser beam at the water surface. All submerged LiDAR points have to be corrected
11 for the refraction, but in order to do so, the water depth must be known for each point.
12 This sets a requirement of modelling the water surface before the refraction correction
13 can be performed. The general processing procedure is well defined; however, there is
14 no standard or universal approach for how to deal with these steps. LiDAR companies
15 have their workflows, but the specific steps in their workflow are usually hidden, which
16 make them non-repeatable.

17 In particular, there is no definitive method for detecting a water surface from green
18 topobathymetric LiDAR data. Often the water surface is detected from simultaneous
19 collection of green and NIR LiDAR measurements, where the green laser reflects from
20 the seabed and the NIR laser reflects from the air-water interface, and the NIR laser data
21 are then used to detect and model the water surface (Allouis et al., 2010; Collin et al.,
22 2008; Guenther, 2007; Parker and Sinclair, 2012). The use of NIR LiDAR data for
23 water surface detection has been applied in several studies. For instance, Hofle et al.
24 (2009) proposed a method for mapping water surfaces based on the geometrical and
25 intensity information from NIR LiDAR data. Su and Gibeaut (2009) classified water
26 points from NIR LiDAR based on point density, intensity and altitude. They identified
27 the shoreline based on the large sudden decrease in NIR LiDAR intensity values when
28 going from land to water. Brzank et al. (2008) used the same three variables (point
29 density, intensity and altitude) in a supervised fuzzy classification to detect the water
30 surface in a section of the Wadden Sea. Another study in the Wadden Sea by Schmidt et
31 al. (2012) used a range of geometric characteristics as well as intensity values to classify
32 water points from NIR LiDAR data.

1 The capability of NIR LiDAR data for water surface detection is thus well documented.
2 However, deriving all the information (seabed and water surface) from a single green
3 LiDAR dataset would be a more effective solution for water surface detection, with
4 respect to the financial expenses and for the difficulties of storing and handling often
5 very large amounts of data. For this purpose, the Austrian LiDAR company RIEGL
6 have developed a software, *RiHYDRO* (RIEGL, 2015), in which it is possible to model
7 the water surface in a two-step approach: 1) Classification of water surface points based
8 on areas with two layers (water surface and seabed) and extending the classification to
9 the entire water body, and 2) Generation of a geometric gridded water surface model for
10 each flight swath based on the classified water surface points. However, *RiHYDRO* is
11 commercial software, and thus the algorithms, which form the basis of the classification
12 and water surface modelling, are not publicly available. Other software packages, such
13 as *HydroFusion* (Optech, 2013) and *LiDAR Survey Studio* (Leica, 2015), also proclaim
14 to have incorporated methods for the entire data processing workflow, but the
15 algorithms in these software packages are also closed and cannot be accessed by users.

16 Only few research studies have investigated the potential of water surface detection
17 from green LiDAR data. Guenther et al. (2000) even regarded water surface detection
18 from green LiDAR data as unacceptable and they justified it with two fundamental
19 issues: 1) No water surface returns are detected in the dead zone, and 2) Uncertainty of
20 the water surface altitude, because the green water surface returns are actually a mix of
21 returns from the air/water interface and from volume backscatter returns, and they are
22 generally found as a cloud of points below the water surface. Mandlbürger et al. (2013)
23 addressed the second issue by comparing the water surface points of NIR and green
24 LiDAR data, and they concluded that it is possible to derive the water surface altitude
25 from the green LiDAR data with sub-decimetre vertical precision relative to a reference
26 water surface derived by the NIR LiDAR data. However, their work addressed only the
27 determination of the water surface altitude, without going into detail on the actual
28 procedure of modelling the water surface. An approach for modelling the water surface
29 from green LiDAR data was presented by Mandlbürger et al. (2015), who did their
30 study in a riverine environment with only few return signals from the water surface.
31 Their method was based on manual estimates of the water level in a series of river cross
32 sections, after which interpolation between the cross sections filled out the gaps with no

1 water surface points to derive a continuous water surface model. The vertical accuracy
2 of the detected water surface was evaluated by statistical comparison against water
3 surface points from a terrestrial laser scanner, resulting in a root mean square error of
4 ± 3.3 cm.

5 Published literature that deals with water surface modelling/detection procedure in the
6 coastal zone based solely on green laser Lidar data are very few and the procedure for
7 LiDAR data processing to reach this goal is not clearly explained.

8 The aim of this study was to investigate the potential of improving the processing
9 procedure of green LiDAR data for generating DEMs in tidal coastal environments
10 characterised by land-water transition zones, and of improving the classification of
11 morphological units in such environments. More specifically, the objectives were:

- 12 1. To develop a robust, repeatable and user friendly processing procedure of raw
13 green LiDAR data for generating high resolution DEMs in land-water transition
14 zones.
- 15 2. To quantify the accuracy and precision of the green LiDAR data based on object
16 detection.
- 17 3. To automatically classify morphological units based on morphometric analyses
18 of the generated DEM.

19 The investigations were based on studies undertaken in a section of the Knudedyb tidal
20 inlet system in the Danish Wadden Sea.

21

22 **2 Study area**

23 The Knudedyb tidal inlet system is located between the barrier islands of Fanø and
24 Mandø in the Danish Wadden Sea (Fig. 2A). The tidal inlet system is a natural
25 environment without larger influence from human activity. The tides in the area are
26 semi-diurnal, with a mean tidal range of 1.6 m, and the tidal prism is in the order of
27 $175 \cdot 10^6$ m³ (Pedersen and Bartholdy, 2006). The main channel is approximately 1 km
28 wide and with an average water depth of approx. 15 m (Lefebvre et al., 2013).

29 The study site is an elongated 3.2 km² (0.85×4 km) section of the Knudedyb tidal inlet
30 system (Fig. 2B). The section is located perpendicular to the main channel and stretches
31 across both topography and bathymetry. The study site extends towards north into an

1 area on Fanø with dispersed cottages (Fig. 2C). The most prominent morphological
2 features within the study site include beach dunes (Fig. 2D), small mounds (Fig. E),
3 swash bars (Fig. 2F-G) and linear bars (Fig. 2H). The quality of the LiDAR data were
4 validated at two sites along Ribe Vesterå River (Fig. 2I-J):

- 5 • Validation site 1 is a cement block with a size of 2.50×1.25×0.80 m located on
6 land next to the mouth of Ribe Vesterå River (Fig. 2I). The block was used for
7 assessing the accuracy and precision of the LiDAR data.
- 8 • Validation site 2 is a steel frame with a size of 0.92×0.92×0.30 m located in the
9 river with the surface just below the water surface (Fig. 2J). The frame was used
10 for precision assessment, and for testing the feature detection capability of the
11 LiDAR system. According to the hydrographic survey standards presented by
12 the International Hydrographic Organization (IHO, 2008), cubic features of at
13 least 1 m² should be detectable in Special Order areas, which are areas with very
14 shallow water as in the study site.

16 **3 Methods**

17 **3.1 Surveys and instruments**

18 LiDAR data and ortophotos were collected by Airborne Hydro Mapping GmbH (AHM)
19 during two surveys on 19 April 2014 and 30 May 2014.

20 On 19 April 2014, validation sites 1 and 2 were covered for accuracy and precision
21 assessment of the LiDAR data by object detection of the block and the frame (for
22 location see Fig. 2). The block was covered by 7 swaths retaining 227 LiDAR points
23 from the block surface. The frame was covered by 4 swaths retaining 46 LiDAR points
24 from the surface of the frame. Ground control points (GCPs) were measured for the four
25 corners of the block with accuracy better than 2 cm using a Trimble R8 RTK GPS.
26 Measurements were repeated three times and averaged to minimize errors caused by
27 measurement uncertainties. GCPs were also collected for the frame; however, during
28 the LiDAR survey the frame experienced an unforeseen intervention by local fishermen
29 using the frame as fishing platform. Therefore, the frame is only used to assess the

1 deviation between the LiDAR points (the precision), and not to assess the deviation
2 between the LiDAR points and GCP's (the accuracy).

3 On 30 May 2014, the study site was covered by 11 swaths, which were used for
4 generating the DEM. Low tide was -1 m DVR90, measured at Grådyb Barre, approx. 20
5 km NW of the study site.

6 The weather conditions were similar during the two surveys, with sunny periods,
7 average wind velocities of 7-8 m/s (DMI, 2014) and approx. 0.5 m wave heights coming
8 from NW, measured west of Fanø (DCA, 2014). The wave heights in the less exposed
9 Knudedyb tidal inlet was observed in the LiDAR data to 0.2-0.3 m. Overall, both days
10 constituted good conditions for topobathymetric LiDAR surveys.

11 In both surveys, LiDAR data were collected with a RIEGL VQ-820-G topobathymetric
12 airborne laser scanner. The scanner is characterized by emitting green laser pulses with
13 532 nm wavelength and 1 ns pulse width. It has a very high laser pulse repetition rate of
14 up to 520,000 Hz, and a beam divergence of 1 mrad creates a narrow laser beam
15 footprint of 40 cm diameter at a flying altitude of 400 m (RIEGL, 2014), which was the
16 actual flying altitude during the surveys. The high repetition rate and narrow footprint
17 makes it well suited to capture fine-scale landforms (Doneus et al., 2013; Mandlbürger
18 et al., 2011; RIEGL, 2014). An arc shaped scan pattern results in a swath width of
19 approx. 400 m (at 400 m flying altitude), while maintaining an almost constant 20°
20 ($\pm 1^\circ$) incidence angle of the laser beam when it penetrates the water surface (Niemeyer
21 and Soergel, 2013). The typical water depth penetration of the laser scanner is 1 Secchi
22 disc depth.

23 For each returned signal, the collected LiDAR data contained information of x, y and z,
24 as well as a GPS time stamp and values of the amplitude, reflectance, return number,
25 attribute and laser beam deviation (RIEGL, 2012).

26 **3.2 Processing raw topobathymetric LiDAR data into a gridded DEM**

27 The essential processing steps, which are standard procedure when processing
28 topobathymetric LiDAR data, were followed to produce a DEM in the study area. These
29 steps included:

- 30 1. Determination of flight trajectory.

- 1 2. Boresight calibration: Calculating internal scanner calibration.
- 2 3. Collecting topobathymetric LiDAR data.
- 3 4. Swath alignment based on boresight calibration: The bias between individual
- 4 swaths was minimized.
- 5 5. Filtering: The raw data contained noise located both above and below ground,
- 6 which needed to be filtered from the point cloud.
- 7 6. Water surface detection: A water surface had to be established in order to correct
- 8 for refraction in the following step.
- 9 7. Refraction correction: All the points below the water surface were corrected for
- 10 the refraction of the laser beam.
- 11 8. Point cloud to DEM: The points were transformed into a surface representing the
- 12 real world topography and bathymetry.

13 Step 1 and 2 were performed prior to the LiDAR survey. The different instruments
14 (LiDAR, IMU and GPS) were integrated spatially by measuring their position relative
15 to each other, when mounted on the airplane, and temporally by calibrating their time
16 stamps.

17 Step 3 was the actual LiDAR survey and step 4 was the initial processing step after the
18 LiDAR survey. The bias between the swaths was minimized in the software
19 RiPROCESS (RIEGL LMS) by automatically searching for planes in each swath and
20 then matching the planes between the swaths.

21 Step 5-8 represents the processing of the point cloud into a DEM. The methods involved
22 in these steps are the main focus in this work and they are described in detail in the
23 following sub-sections. Each swath was pulled individually through the processing
24 workflow to account for the continually changing water level in the study area due to
25 tides.

26 **3.2.1 Filtering**

27 The raw LiDAR data contained noise in the air column originating from the laser being
28 scattered by birds, clouds, dust and other particles, and noise was also appearing below
29 the ground/seabed (Fig. 3A-B). This noise had to be filtered before further processing.
30 The filtering process involved both automatic and manual filtering.

1 1. Automatic filtering

2 The automatic filtering was carried out in HydroVish (AHM) with the tool *Remove flaw*
3 *echoes* (Fig. 3C). The filtering tool was controlled by three variable parameters: search
4 radius, distance and density. The search radius parameter specified the radius of a
5 sphere in which the distance and density filters were utilized. The distance parameter
6 rejected a point, if it was too far from any other point within the sphere. The density
7 parameter specified the lower limit of points within the sphere. The automatic filter
8 iterated through all the points in the point cloud.

9 In order to identify the best settings of the three parameters, a sensitivity analysis was
10 performed on three data fragments representing different natural environments in the
11 Knudedyb tidal inlet system: a fragment in the flood channel, one on the tidal flat and a
12 fragment with vegetation. The outcome of the filtering was compared for different
13 settings to decide the most suitable settings to use for filtering the whole study area. It
14 was not possible to reach a specific setting, which would be optimal for all the different
15 environments. Particularly, the deeper bathymetric parts contained more widely
16 dispersed points, which were easily rejected by the filter. The analyses with different
17 settings also showed that two layers of noise close to the ground, both above and below,
18 were very difficult, if not impossible, to reject with this automatic filtering method. The
19 settings were selected so that a minimum of valid points were rejected by the automatic
20 filter. The settings were: Search radius = 1 m, distance = 0.75 m and density = 4.

21 2. Manual filtering

22 The remaining noise was manually filtered in the software Fledermaus (QPS) (Fig. 3D).

23 The filtered point cloud (with water points) was used in the following step to detect the
24 water surface. Meanwhile, a copy of the data were undergoing additional manual
25 filtering, removing all the water points (Fig. 3E). After this final filtering step, there
26 were only points representing topography, bathymetry, vegetation and man-made
27 structures left in the dataset.

28 **3.2.2 Water surface detection**

29 The water surface detection was based on determining the water surface *altitude* and the
30 water surface *extent*. The water surface altitude was determined based on the water

1 surface points and the extent was determined by extrapolating the water surface until it
2 intersected the surface of the topography. Two assumptions about the water surface
3 were made:

- 4 1. The water surface was horizontal. This was a simplification of the real world.
5 Tidal processes and wind- and wave-setup may cause the water surface to be
6 sloping, and the water is often topped by more or less significant wave action. A
7 linear fit through the water surface LiDAR points along the main channel,
8 showed a changing water level of 0.13 m over a distance of 400 m,
9 corresponding to a 0.325×10^{-3} (0.019 deg.) sloping water surface. A similar fit
10 through the LiDAR points along the flood channel showed a slope of 0.156×10^{-3}
11 (0.009 deg.). The maximum wave heights observed in the main channel were
12 20-30 cm. Based on the moderate slope of the water surface and relatively low
13 wave height, the water surface was assumed flat. This assumption is deemed
14 error prone, but at the time of this study, it was currently our best estimate.
- 15 2. The study area contained water bodies with two different water levels: One
16 represented the water level in the main channel and the other represented the
17 water level in the flood channel. This was also a simplification, as the tidal flat
18 contained small ponds with potentially different water levels. However, almost
19 all of these ponds contained no LiDAR points of the water surface, which means
20 that the water depth in the ponds must have been within the limitation of the
21 dead zone. Therefore, it was impossible to detect individual water surfaces in the
22 ponds.

23 A series of processing steps were performed to detect the water surface. The first step
24 was to extract a *shallow surface* and a *deep surface* from the filtered point cloud (with
25 water points) in Fledermaus (Fig. 3F). Both surfaces consisted of 0.5×0.5 m cells, and
26 the altitude of each cell was equal to the highest point within the cell (shallow surface)
27 and the lowest point within the cell (deep surface), respectively. The shallow surface
28 should then display the topography along with the water surface, whereas the deep
29 surface should display the topography and the seabed (as long as the seabed was
30 detected by the laser). It is worth noting, that the extraction of the shallow surface and
31 the deep surface have nothing to do with the final DEM, as they are just intermediate
32 steps performed for the water surface detection.

1 The following steps were focused on the shallow surface to determine the altitude of the
2 water surface (Fig. 3G). First, the shallow surface was down-sampled to a surface with a
3 cell size of 2×2 m, and the new cells were populated with the maximum altitude of the
4 input cells. The down-sampling was done for smoothing the water surface, and thereby
5 eliminating most of the outliers. The exact cell size of 2×2 m, as well as populating
6 them with the maximum value, was chosen based on the work by Mandlbürger et al.
7 (2013). They compared water surface detection capability between green LiDAR data,
8 collected with the same RIEGL-VQ-820-G laser scanner, and NIR LiDAR data, which
9 was assumed to capture the true water surface. They found that the green LiDAR
10 generally underestimated the water surface level, but that reliable results were achieved
11 by increasing the cell size and only taking the top 95-100% of water points into account.
12 According to their work, it was assumed that placing the water surface on the highest
13 points in 2 m cells provided a good estimate of the true water level. However, based on
14 their results it could be expected that the water surface level in this case would be
15 underestimated in the order of 2-4 cm.

16 The water covered areas in the main channel and the flood channel were manually
17 extracted from the newly down-sampled raster surface. The average altitude of the cells
18 was calculated individually in each area, and these values constituted the water surface
19 levels in the main channel and in the flood channel, respectively.

20 Hereafter, the extent of the water surfaces was determined (Fig. 3H). Two horizontal
21 water surfaces were created in the flood channel and the main channel with a cell size of
22 0.5×0.5 m and cell values equal to the determined water surface altitudes in each
23 region. The high spatial resolution of 0.5 m cells was chosen to produce a detailed water
24 surface along the edges of the land-water transition. It also made the calculations in the
25 following step straightforward, because the resolution was similar to that of the deep
26 surface. The deep surface cell altitudes were subtracted from the water surface altitude
27 and all cells with resulting negative values were discarded from the water surface.
28 Thereby, all the water surface cells which were below the deep surface were discarded.
29 All the cells above the deep surface were expected to represent the two water surfaces.
30 Thereby, two water surfaces were created; one in the main channel and one in the flood
31 channel.

1 **3.2.3 Refraction correction**

2 The refraction correction of all the points below the water surfaces was calculated in
3 HydroVish (AHM). The input parameters were the filtered point cloud (without water
4 points), the derived water surfaces and the trajectory data of the airplane. These were all
5 converted to F5 file format to allow import into HydroVish (AHM). The refraction
6 correction was calculated automatically for each point based on the water depth, the
7 incident angle of the laser beam, and the refracted angle according to Snell's Law (Eq. 1
8 and Fig. 3I).

9 **3.2.4 Point cloud to DEM**

10 After iterating through the processes of filtering, water surface detection and refraction
11 correction for all the individual swaths, the LiDAR points of all swaths were combined.
12 The transformation from point cloud into a DEM was performed with ArcGIS (ESRI)
13 software. The DEM was created as a raster surface with a cell size of 0.5×0.5 m, and
14 each cell was attributed the average altitude of the points within the cell-boundaries. It
15 was chosen to make the resolution of the DEM lower than the laser beam footprint size
16 (i.e. 40 cm), due to the inaccuracies arising from attributing smaller cells with measured
17 altitude values spanning across a larger area. Furthermore, the 0.5 m cell size was
18 chosen to get as high resolution as possible without making any significant interpolation
19 between the measurements. In this way, each cell represented actually measured
20 altitudes instead of interpolated values. However, there were still very few gaps of
21 individual cells with no data in the resulting raster in areas with relatively low point
22 density. Despite of the general intention of avoiding interpolation it was chosen to
23 populate these cells with interpolated values to end up with a full DEM coverage
24 (except for the bathymetric parts beyond the maximum laser penetration depth). The
25 arguments for interpolation were that 1) the interpolated cells were scattered and
26 represented only 1.7 % of all the cells, 2) they were found primarily on the tidal flat
27 where the slope is generally less than 1° , meaning that the altitude difference from one
28 cell to a neighbouring cell is usually less than 1 cm, and 3) the general point density in
29 most of the study area was so high that the loss of information by lowering the DEM
30 resolution would represent a larger sacrifice than interpolating a few scattered cells. The
31 interpolation was performed by assigning the average value of all neighbouring cells to

1 the empty cells. The final DEM was thereby fully covering the topography, and the
2 bathymetry was covered down to a depth equal to the maximum laser penetration depth.

3 **3.3 Accuracy and precision of the topobathymetric LiDAR data**

4 The term *accuracy* refers to the difference between a point coordinate (in this case a
5 LiDAR point) compared to its “true” coordinate measured with higher accuracy, e.g. by
6 a total station or a differential GPS; while the term *precision* refers to the difference
7 between successive point coordinates compared to their mean value, i.e. the
8 repeatability of the measurements (Graham, 2012; Jensen, 2009; RIEGL, 2014).

9 Two “best-fit planes” based on the LiDAR points on the block and the frame surfaces
10 were established with the *Curve Fitting tool* in MATLAB (MathWorks). We propose
11 the use of these two planes to give an indication of the relative precision of the LiDAR
12 measurements.

13 Another best-fit plane was established based on the block GPS measurements, and this
14 plane was regarded as the “true” block surface for assessment of the accuracy of the
15 LiDAR measurements. The established planes were described by the polynomial
16 equation:

$$17 \quad z(x, y) = a + bx + cy \quad (2)$$

18 where x , y and z are coordinates and a , b and c are constants. Inserting x and y
19 coordinates for the LiDAR surface points in Eq. (3) led to a result of the corresponding
20 altitude (z) as projected on the fitted plane. The difference between the altitude of the
21 LiDAR point and the corresponding altitude on the fitted plane was used as a measure
22 of the vertical accuracy (for the GCP fitted plane of the block) and the vertical precision
23 (for the LiDAR point fitted plane of the block and the frame). Statistical measures of the
24 standard deviation (σ), mean absolute error (E_{MA}), and root mean square error (E_{RMS})
25 were calculated by:

$$26 \quad \sigma = \sqrt{\frac{\sum(z_i - z_{\text{plane}})^2}{n-1}} \quad (3)$$

$$27 \quad E_{MA} = \frac{\sum|z_i - z_{\text{plane}}|}{n} \quad (4)$$

1
$$E_{\text{RMS}} = \sqrt{\frac{\sum(z_i - z_{\text{plane}})^2}{n}}$$
 (5)

2 where z_i is the altitude of the measured LiDAR points, z_{plane} is the corresponding
3 altitude on the best-fit plane, and n is the number of LiDAR points. The vertical
4 accuracy and precision were determined at a 95% confidence level based on the
5 accuracy standard presented in *Geospatial Position Accuracy Standards Part 3:*
6 *National Standard for Spatial Data Accuracy* (NSSDA) (FGDC, 1998):

7
$$CI_{95\%} = E_{\text{RMS}} \cdot 1.96$$
 (6)

8 The horizontal accuracy was determined as the horizontal mean absolute error ($E_{\text{MA,xy}}$)
9 based on the horizontal distances between the block corners, measured with RTK GPS,
10 and the best approximation of the block corners derived from the LiDAR points of the
11 block surface. The minimum distance between a block corner and the perimeter of the
12 LiDAR points was regarded as the best approximation. Hereafter $E_{\text{MA,xy}}$ was calculated
13 as the average of the four corners.

14 **3.4 Geomorphometric and morphological classifications**

15 The processed DEM was applied in two classification analyses; first a *geomorphometric*
16 classification and then a *morphological* classification. Both were based on the DEM and
17 derivatives of the DEM, but they differentiated by the resulting classification classes,
18 which showed 1) Surface geometry and 2) Surface morphology.

19 Geomorphometric classification analysis

20 The tool Benthic Terrain Modeler (BTM) (Wright et al., 2005) was used for the
21 geomorphometric classification. The tool is an extension to ArcGIS Spatial Analyst,
22 originally used for analysing MBES data (Diesing et al., 2009; Lundblad et al., 2006;
23 Rinehart et al., 2004). The BTM classification tool uses fine- and broad scale
24 Bathymetric Positioning Indexes (BPIs) (Verfaillie et al., 2007) in a multiple scale
25 terrain analysis to classify fine- and broad scale geometrical features. The BPIs are
26 measures of the altitude of a cell compared to the altitude of the surrounding cells
27 within the determined scale (radius) size. Positive BPI values indicate a higher altitude
28 than the neighbouring cells and negative BPI values indicate a lower altitude than the
29 neighbouring cells. For instance, a BPI value of 100 corresponds to 1 standard deviation

1 and a value of -100 corresponds to -1 standard deviation. BPI values close to zero are
2 derived from flat areas or from constant slopes.

3 The altitude of the DEM was exaggerated 10 times before the classification, to enable
4 the BTM to detect the shapes of the landscape. The fine- and broad scales were
5 determined based on the BPI results for different radius sizes. The best results were
6 obtained from a broad scale BPI of 100 m radius and a fine scale BPI of 10 m radius.
7 The fine- and broad scale BPIs were used, together with DEM derived slopes to classify
8 the investigated area into the geomorphometric classes: Small-scale crests, large-scale
9 crests, depressions, slopes and flats (Fig. 4). The classification classes were decided
10 based on previous studies using the BTM classification tool with success (Diesing et al.,
11 2009; Lundblad et al., 2006). The thresholds for the fine- and broad scale BPIs were in
12 previous studies often defined as 1 standard deviation (Lundblad et al., 2006; Verfaillie
13 et al., 2007), however, thresholds of 0.5 standard deviations have also previously been
14 applied (Kaskela et al., 2012). We used a low threshold of 0.5 standard deviations due
15 to the generally very gentle variations in the landscape geometry of the tidal inlet
16 system. We defined the threshold between slopes and flats as 2°. This definition was a
17 compromise between detecting as many slopes as possible but avoiding too many “false
18 slopes” being detected along the swath edges, which seemed to be a consequence of
19 lower precision at the outer beams of the swath, as well as differences between
20 overlapping swaths.

21 Morphological classification analysis

22 A morphological classification was developed for the purpose of delineating classes of
23 actual morphological features in the study area. This classification was built partly on
24 different neighbourhood analyses and slopes derived from the DEM, and partly on the
25 local tidal range. Large scale crests from the geomorphometric classification were also
26 incorporated in the analysis. Figure 5 describes the steps performed in ArcGIS, which
27 led to the classification of 6 morphological classes: Swash bars, linear bars, beach
28 dunes, intertidal flats, intertidal creeks and subtidal channels. All the criteria for
29 defining a particular morphological class had to be fulfilled for a cell to be classified
30 into that class.

1 33 years of continuous measurements of the water level at Havneby on Rømø, 25 km
2 south of the study area, shows a mean low water level of -0.94 m (DVR90) and a mean
3 high water of 0.94 m (DVR90) (Klagenberg et al., 2008). Although the tidal range in
4 Knudedyb is probably slightly different, it is the best estimate for the study site.
5 Therefore, these water levels were used to separate between the supratidal, intertidal and
6 subtidal zones.

7 Subtidal channels were defined as everything below the mean low water, which is -0.94
8 m. A “smooth DEM” was created, in which each cell of the original DEM was assigned
9 the average altitude value of its surrounding cells in a window size of 100x100 m. The
10 result was subtracted from the original DEM, creating an Elevation Change Model
11 (ECM), which made it possible to extract information about the deviation of the cells in
12 the DEM compared to its surrounding cells. The principle is similar to the BPI, and
13 again the purpose was to locate cells, with a higher/lower altitude than its surrounding
14 cells. Positive values were higher cells and negative values were lower cells. Certain
15 thresholds were found suitable for classifying beach dunes (> 0.8 m) and intertidal
16 creeks (< -0.3 m). These two classes were furthermore classified into their respective
17 tidal zones (supratidal and intertidal) based on the altitude. Intertidal flats were
18 classified by low slope values ($< 1^\circ$) of a down-sampled 2 m DEM (each down-sampled
19 cell was assigned the mean value of its 4x4 original cells). Moreover, to be classified as
20 a flat, the ECM has to be within ± 10 cm to avoid any incorrect intertidal flat
21 classification of flat crests on top of bars or flat bottoms inside creeks or channels. The
22 BTM classification class “large-scale crests” is used as an input, since it is found to
23 capture bar features. However, the thresholds used in the BTM classification resulted in
24 capturing features larger than bars in the large-scale crests class. To distinguish between
25 bars and larger features, the standard deviation of each DEM cell in a moving window
26 size of 250x250 m is calculated. A suitable threshold to distinguish between bars and
27 larger features are 0.6 standard deviations. Finally, swash bars and linear bars are
28 distinguished by an area/perimeter-ratio, based on the assumption that linear bars has a
29 smaller ratio than swash bars, due to the different shapes. In this case, 4 were found to
30 be a suitable ratio threshold.

31

1 4 Results

2 4.1 Refraction correction and dead zone extent

3 The vertical adjustment of the LiDAR points due to refraction correction (z_{diff}) is
4 linearly correlated with the water depth (d) (Fig. 6). An empirical formula was derived
5 for this relationship and is given by the equation:

$$6 \quad z_{\text{diff}} = 0.227 * d, R^2 = 0.997 \quad (7)$$

7 A LiDAR point at 1 m water depth is vertically adjusted by approximately 0.23 m (Fig.
8 6). The variations around the linear trend in Fig. 6 are due to changing incidence angles
9 of the laser beam that varies with the airplane attitude (roll, pitch and yaw).

10 The vertical extent of the dead zone is approx. 28 cm, determined by plotting the
11 vertical difference between the shallowest and the deepest LiDAR point within 0.5 m
12 cells – i.e. between the shallow surface and the deep surface (Fig. 7). The difference is
13 manifested by an abrupt change at the dead zone, and the highest rate of change is
14 shown to be at a water depth of approx. 28 cm.

15 4.2 Sub-decimetre accuracy and precision

16 The vertical root mean square error of the LiDAR data is ± 4.1 cm, and the accuracy is
17 ± 8.1 cm with a 95% confidence level (Table 1 and Fig. 8A). The vertical precision of
18 the LiDAR data with a 95 % confidence level is ± 3.8 cm for the points on the frame,
19 and ± 7.6 cm for the points on the block (Table 1).

20 The horizontal accuracy calculated as the horizontal mean absolute error ($E_{\text{MA},xy}$) is
21 determined to ± 10.4 cm, which is the average of the minimum distances between the
22 four block corners and the edge of the block surface derived by the LiDAR data (Fig.
23 8B).

24 4.3 Point density and resolution

25 The average point density is 20 points per m^2 , which equals an average point spacing of
26 20 cm (Table 2). The point density of the individual swaths varies between 7-13 points

1 per m², and the point density of the combined swaths in the study area, varies between
2 0-216 points per m², although above 50 points per m² are rare.

3 **4.4 DEM and landforms**

4 The altitudes in the studied section of the Knudedyb tidal inlet system range from -4
5 m DVR90 in the deepest parts of the flood channel and main channel to 21 m DVR90
6 on top of the beach dunes on Fanø (Fig. 9). Beach dunes and cottages of the village
7 Sønderho are clearly visible in the northern part of the study site (Fig. 9A-B). The
8 intertidal areas are generally flat, while the most varying morphology is found in the
9 area of the flood channel (Fig. 9C-D), and in the area close to the main channel (Fig.
10 9E-F). The flood channel is approximately 200 m wide in the western part and it divides
11 into two channels towards east. The bathymetry of the channel bed is clearly captured
12 by the LiDAR data in the eastern part, and also in the western part down to -4 m
13 DVR90, which approximately equals a water depth of 3 m at the time of survey. An
14 intertidal creek joins the flood channel from the north (Fig. 9D). From the flood channel
15 towards south, the tidal flat is vaguely upward sloping, until reaching two distinct swash
16 bars, which are rising 0.9 m above the surrounding tidal flat, reaching a maximum
17 altitude of 1.5 m DVR90 (Fig. 9E-F). Further south, the linear bars along the margin of
18 the main channel are clearly captured in the DEM (Fig. 9E).

19 **4.5 Geomorphometric and morphological classifications**

20 The geomorphometric and morphological classifications show that most of the study
21 site is located in the intertidal zone, and is mostly flat. That is manifested by the
22 dominating two classes; flats and intertidal flats (Fig. 10A-B). The geomorphometric
23 classification identifies slopes as stripes with NNW-SSE directionality across the flats.
24 These are following the direction of the survey lines, and thus, they are not real
25 morphological features but more an indication of lower precision of the LiDAR data,
26 especially at the outer beams of the swath. These swath artefacts are smoothed out in the
27 morphological classification by down-sampling the DEM to 2 m resolution, and
28 therefore, the intertidal flats appear uniform and seamless. The bar features close to the
29 main channel are well defined in the geomorphometric classification where they are
30 classified as large-scale crests and small-scale crests surrounded by slopes. In the

1 morphological classification, these are identified based on neighbourhood analyses and
2 separated by the area/perimeter-ratio into two classes, swash bars and linear bars (Fig.
3 10C). Large-scale crests are also found on Fanø in the northern part of the area, and
4 most of these are classified as beach dunes in the morphological classification. The
5 geomorphometric classification identifies more large-scale crests along the banks of the
6 flood channel, however, these are not actual bar features but they are identified as crests
7 due to the nearby flood channel and creeks resulting in a positive broad scale BPI. In the
8 morphological classification it is possible to distinguish between these “false” crests and
9 actual bar features, by looking at altitude deviations at an even larger scale than the
10 broad scale BPI. The intertidal creek in the NWern part of the area is a mix of
11 depressions, slopes and small-scale crests in the geomorphometric classification,
12 whereas it is relatively well defined and properly delineated in the morphological
13 classification (Fig. 10D).

14 The geomorphometric classification identifies slopes along the banks of the main
15 channel, flood channel and the intertidal creek, as well as in front of the beach dunes
16 and along the edges of the swash bars and linear bars. The slopes seem particularly
17 reliable at delineating the features in the intertidal zone; swash bars, linear bars and
18 creeks. Depressions are primarily identified in the deepest detected parts of the main
19 channel and in the flood channel, in the intertidal creek and in the beach dunes. Small-
20 scale crests are found in the geomorphometric classification in locations which are high
21 compared to its near surroundings. They are primarily seen as parts of the linear bars
22 close to the main channel, in the beach dunes on Fanø and along the banks of the
23 intertidal creeks.

24 A few small circular patches of approx. 5 m diameter with *Spartina Townsendii*
25 (Common Cord Grass) located on the intertidal flat are classified as small-scale crests in
26 the geomorphometric classification (Fig. 11). It clearly shows the capability of
27 capturing relatively small features in the DEM and in the derived classification.

28

1 **5 Discussion**

2 **5.1 Performance of the water surface detection method**

3 The water surface in topobathymetric LiDAR surveys is most often detected from NIR
4 LiDAR data, which is simultaneously collected along with the green LiDAR data
5 (Collin et al., 2012; Guenther et al., 2000; Parker and Sinclair, 2012; Wang and Philpot,
6 2007). However, detecting the water surface based on the green LiDAR data provides a
7 potential to perform topobathymetric surveys with just one sensor, thus optimizing the
8 survey costs as well as data handling and storage.

9 The two critical issues risen by Guenther et al. (2000), as mentioned in the introduction,
10 concerning the water surface detection with green LiDAR were thoroughly investigated
11 in this study. The first issue, regarding the gap of detected water surface signals in the
12 dead zone, is addressed by detecting the water surface based on areas which are known
13 to be covered by water, and thereafter extending the water surface until it intersects the
14 topography, so that also the dead zone is covered by the modelled water surface. The
15 second issue, regarding uncertainty in the water surface altitude determination, is
16 addressed using the results presented by Mandlbürger et al. (2013) who found a
17 statistical relationship between the cloud of water surface points in the green LiDAR
18 data and the water surface altitude derived from NIR LiDAR data. Mandlbürger et al.
19 (2013), however, did not describe the actual method of modelling the water surface,
20 which is done in this study. Mandlbürger et al. (2015), on the other hand, did propose a
21 method for modelling the water surface, however, it was in a fluvial environment and
22 the water level was based on manual determinations of cross sectional water levels. The
23 water surface detection method in this study is thus new in combining the properties: 1)
24 It is only using green LiDAR data, 2) it is based on automatic water level determination
25 3) it is applied in a tidal environment (can be applied in any coastal environment) and 4)
26 it is open to the public and described in detail.

27 The developed water surface detection method is new but it must be pointed out that the
28 assumption of a flat water surface leaves room for improvements for the future,
29 especially if it is applied in a fluvial environment. Assuming a flat water surface is
30 indeed a simplification of the real world, since the water surface in reality can be
31 inclined, and it can be topped by waves.

1 **5.2 Implications of the dead zone**

2 The vertical extent of the dead zone is in this study determined to approx. 28 cm (Fig.
3 7), which means that no return signal is detected from the water surface when the water
4 depth is less than 28 cm. As Guenther et al. (2000) explains, the dead zone poses a real
5 challenge to the modelling of a water surface, because all submerged points, also those
6 in less than 28 cm water depth, have to be corrected for refraction. With the water
7 surface detection method proposed in this work this issue has been dealt with by
8 extending the water surface into the dead zone, which makes it possible to correct the
9 LiDAR points in 0-28 cm water depth for refraction. In this way, the implication of the
10 dead zone along the channel edges is diminished, which is particularly beneficial in flat
11 areas such as the Knudedyb tidal inlet system, where the dead zone may cover large
12 areas depending on the tide (Fig. 12).

13 The implication of the dead zone along the channel edges is minimised, but the setting
14 is different for the small ponds on the intertidal flats. They may have different water
15 levels than in the large channels, but no detected water surface points, since the water
16 depth in the ponds are generally less than the vertical extent of the dead zone, i.e.
17 approx. 28 cm. The presented method is not capable of detecting a water surface in
18 these ponds, which means that the bottom points of the ponds are not corrected for
19 refraction. According to the calculated refraction (Fig. 6), omitting refraction correction
20 of a 28 cm deep pond will result in -6 cm altitude error (naturally less error in shallower
21 water).

22 **5.3 Evaluation of the topobathymetric LiDAR data quality**

23 The vertical accuracy of conventional topographic LiDAR has previously been
24 determined to ± 10 -15 cm (Hladik and Alber, 2012; Jensen, 2009; Klemas, 2013; Mallet
25 and Bretar, 2009). Only few previous studies have focused on the accuracy of shallow
26 water topobathymetric LiDAR data (Mandlbürger et al., 2015; Nayegandhi et al., 2009;
27 Steinbacher et al., 2012). Nayegandhi et al. (2009) determined the vertical E_{RMS} of
28 LiDAR data in 0-2.5 m water depth to ± 10 -14 cm, which is above the ± 4.1 cm E_{RMS}
29 found in this study (Table 1). Steinbacher et al. (2012) compared topobathymetric
30 LiDAR data from a RIEGL VQ-820-G laser scanner with 70 ground-surveyed river
31 cross sections, serving as reference, and found that the system's error range was ± 5 -10

1 cm, which is comparable to the ± 8.1 cm accuracy found in this study. Mandlbürger et al. (2015) compared ground-surveyed points from a river bed with the median of the four nearest 3D-neighbors in the LiDAR point cloud, and they found a standard deviation of 4.0 cm, which is almost equal to the ± 4.1 cm standard deviation found in this study (Table 1). In comparison with these previous findings of LiDAR accuracy, the assessment of the vertical accuracy in this study indicates a good quality of the LiDAR data.

8 Mapping the full coverage of tidal environments, such as the Wadden Sea, require a combination of topobathymetric LiDAR to capture topography and shallow bathymetry and MBES to capture the deeper bathymetry. The two technologies make it possible to produce seamless coverage of entire tidal basins; however, merging the two products raises the question whether the quality of the data from the two different sources is comparable. Comparing the LiDAR accuracy with previous findings of accuracy derived from MBES systems indicates similar or slightly better accuracy from the MBES systems (Dix et al., 2012; Ernstsen et al., 2006a). Dix et al. (2012) determined the vertical accuracy of MBES data by testing the system on different objects and in different environments, and found the vertical E_{RMS} to be ± 4 cm. Furthermore, they tested a LiDAR system on the same objects and found a similar vertical E_{RMS} of ± 4 cm. The vertical E_{RMS} of ± 4.1 cm found in this study is very close to both the MBES accuracy and LiDAR accuracy determined by Dix et al. (2012). Another study by Ernstsen et al. (2006a) determined the vertical precision of a high-resolution shallow-water MBES system based on 7 measurements of a ship wreck from a single survey carried out in similar settings as the present study, namely in the main tidal channel in the tidal inlet just north of the inlet investigated in this study. They found the vertical precision to be ± 2 cm, which is slightly better than the vertical precision of ± 3.8 cm (frame) and ± 7.6 cm (block) found in this study. Overall, accuracy and precision are within the scale of sub decimetres for both topobathymetric LiDAR and MBES systems, which enables the mapping of tidal basins with full coverage and with comparable quality.

30 Due to technical and logistical reasons, the data validation and the actual survey were carried out on different days and in different locations. Based on this, it is a fair question to ask, whether the determined quality actually represents the quality of the data within

1 the study site. In order to address this issue, the environmental conditions between the
2 two surveying dates, as well as the environmental differences, which may impact the
3 data quality, between the study site and the validation sites are compared.

4 The environmental conditions in the two surveying days were similar, with sunny
5 conditions, average wind velocities of 7-8 m/s (DMI, 2014) and significant wave
6 heights, measured west of Fanø at 15 m water, of approx. 0.5 m coming from NW
7 (DCA, 2014). However, the waves in the main channel, next to the study site, have been
8 observed in the 30 May LiDAR point cloud to be not more than 0.2-0.3 m, which can be
9 explained by the location of the study site in lee of the western most intertidal flats and
10 the ebb-tidal delta. The wave heights in the rest of the study area (flood channel and
11 intertidal ponds) were in the scale of sub decimetres. In comparison, there were no
12 waves at validation site 2 in Ribe Vesterå River during the 19 April LiDAR survey. As
13 already mentioned, the proposed water surface detection method has a shortcoming of
14 not modelling the waves, and this is a source of error in areas exposed to waves. The
15 precision of the seabed points within the study area are therefore expected to be worse
16 than the ± 3.8 cm precision determined at validation site 2, because of the larger wave
17 exposure.

18 The water clarity/turbidity impacts the accuracy of the LiDAR data negatively, due to
19 scattering on particles in the water column, which causes the laser beam to spread
20 (Kunz et al., 1992; Niemeyer and Soergel, 2013). Moreover, part of the light is reflected
21 in the direction of the receiver, and such return signals can be difficult to distinguish
22 from the seabed return (Kunz et al., 1992). The turbidity was measured at validation site
23 2 and in the flood channel close to the study site during the 19 April survey by
24 collecting water samples and subsequently analysing the samples for suspended
25 sediment concentration (SSC) and organic matter content (OMC). The analyses showed
26 that the average SSC was higher in the flood channel (17.2 mg/kg) than in the river
27 (10.2 mg/kg). In contrast, the average OMC was lower in the flood channel (25.5 %)
28 than in the river (40.0 %). These observations indicate that 1) the underwater precision
29 is assessed in a location with higher turbidity than the environment within the study site;
30 therefore, the turbidity cannot be a cause of lower precision in the study site, and 2) the
31 penetration depth seems to be controlled by the OMC rather than by the SSC. This is
32 new knowledge, since no previous studies (from what we know) have investigated the

1 relative effect of organic matter as opposed to inorganic matter on the laser beam
2 penetration depth. However, in order to determine the relationship with statistical
3 confidence, a more comprehensive study is needed, involving measurements of
4 penetration depth at different SSCs and OMCs, and without disturbance from other
5 environmental parameters.

6 **5.4 Spatial variations of topobathymetric LiDAR data quality**

7 The quality of spatial datasets is often provided as single values, such as ± 8.1 cm for the
8 vertical accuracy in this case, and then the determined value represents the
9 accuracy/precision of the whole dataset. However, in reality the value is only a measure
10 of the local quality at the location where the assessment is conducted. The quality of the
11 dataset varies spatially, and one way to illustrate that is to extract the maximum vertical
12 difference between the LiDAR points of the processed point cloud within every 0.5×0.5
13 m cell throughout the study site (Fig. 13). In flat areas, without multiple return signals,
14 this shows the spatially varying precision of the dataset. There are large differences on
15 Fanø, which is expected due to vegetation causing multiple LiDAR returns from both
16 the vegetation canopy and from the bare ground. In contrast, the differences on the very
17 gently sloping, non-vegetated tidal flat are up to 10 cm, and there is no simple and
18 natural reason for that variation. A range of factors contribute to the observed
19 variations:

20 Laser beam incidence angle: The incidence angle, at which the laser beam hits the
21 ground/seabed, is determined by a combination of the scan angle, the water surface
22 angle and the terrain slope. The shape of the footprint is stretched with larger incidence
23 angles, and this effect can cause pulse timing errors in the detected signal, which leads
24 to a decreasing vertical accuracy (Baltasvias, 1999). The error associated with larger
25 scan angles is generally causing the outer beams, toward the swath edges, to attain a
26 lower accuracy (Guenther, 2007). This is a reason for the observed variations along the
27 swath edges (Fig. 13). Terrain slopes has the same effect of decreasing the vertical
28 accuracy due to the footprint stretching. The measured altitude tend to be biased toward
29 the shallowest point of the slope within the laser beam (Guenther, 2007). However, the
30 influence of slope is not crucial in the Knudedyb tidal inlet system, since it is generally
31 a very flat area.

1 Vertical bias between overlapping swaths: Areas covered by more than a single swath
2 tend to show more vertical variation in the LiDAR point measurements. This can be
3 caused by variance/error in the GPS measurements and/or IMU errors (Huising and
4 Gomes Pereira, 1998). The vertical bias between swaths has been observed in the point
5 cloud to be up to 5 cm, but it is varying throughout the study site. In most environments,
6 a bias of 5 cm would be unnoticeable, but because of the large and very flat parts of the
7 Knudedyb tidal inlet system, even a small bias becomes readily evident.

8 Water depth: The accuracy and precision are expected to be lower as the laser beam
9 penetrates deeper into the water column (Kunz et al., 1992). The laser beam footprint is
10 diverging as it moves through the water column, resulting in a larger footprint on the
11 seabed. The altitude of the detected point is thus derived from the measurement on a
12 larger area on the seabed, which will decrease the vertical accuracy, as well as decrease
13 the capability of detecting small objects. With this in mind, the lower precision at the
14 frame compared to the block is opposite of what would be expected, since the frame is
15 below water and the block is on land. In this case, other factors, such as overlapping
16 swaths and/or scan angle deviations, have more influence on the precision than the
17 water depth. Also, it should be remembered that the frame surface was close to the
18 water surface, and the effect of the water depth on the precision would most likely be
19 more evident if it was located in deeper water.

20 Additional factors, beside the ones mentioned above, may influence the quality of
21 LiDAR datasets. For instance, a dense vegetation cover of the seabed or breaking waves
22 that makes the laser detection of the seabed almost impossible. However, these factors
23 do not have a great influence in the studied part of the Knudedyb tidal inlet system, and
24 thus they are not further elaborated.

25 **5.5 Evaluation of the morphological classification**

26 The morphological classification presented in this study is based on the studied section
27 of the Knudedyb tidal inlet system. The overall concept of using tidal range, slope and
28 variations of the altitude at different spatial scales proves to be a reliable method for
29 delineating the morphological features in this tidal environment. The concept, however,
30 can be applied in other environments. The specific thresholds in the classification
31 determined in this study may deviate in other areas. Morphological features of different

1 sizes require steps of other spatial scales in the neighbourhood analyses to produce a
2 successful classification. In the future the classification method will be improved by
3 implementing an objective method for determining the scales, which can make it
4 applicable in areas with different morphological characteristics. Such an objective scale
5 determination method is presented by Ismail et al. (2015), who determined the scales
6 based on the variance of the DEM at progressively larger window sizes. In this way, the
7 sizes of the morphological features are determining the scales for the classification.

8 **5.6 Using topobathymetric LiDAR data to map morphology in a highly** 9 **dynamic tidal environment**

10 The study demonstrates the capability of green topobathymetric LiDAR to resolve fine-
11 scale features, while covering a broad-scale tidal inlet system. Collecting
12 topobathymetric LiDAR data with a high point density of 20 points/m² on average
13 enables detailed seamless mapping of large tidal environments, and the LiDAR data has
14 further proved to maintain a high accuracy. The combined characteristics of mapping
15 with high resolution and high accuracy in a traditionally challenging environment
16 provide many potential applications, such as mapping for purposes of spatial planning
17 and management, safety of navigation, nature conservation, or morphological
18 classification, as demonstrated in this study. The developed LiDAR data processing
19 method is tailored to a morphological analysis application. The best representation of
20 the morphology is mapped by gridding the average value of the LiDAR points into a
21 DEM with a 0.5 × 0.5 resolution. Other applications would require different gridding
22 techniques. For instance hydrographers, who are generally interested in mapping for
23 navigational safety, would use the shallowest point for gridding. However, the overall
24 method for processing the point cloud can be used regardless of the application. Only
25 the last and least challenging/time consuming step of gridding the point cloud into a
26 DEM may vary depending on the application.

27 Applying topobathymetric LiDAR data for morphological analyses in tidal
28 environments enables a holistic approach of seamlessly merging marine and terrestrial
29 morphologies in a single dataset. In order to map the morphology of tidal environments
30 in full coverage, however, a combination of topobathymetric LiDAR and MBES swath
31 data is required. The comparable quality and resolution of LiDAR and MBES data gives

1 a potential to map large scale tidal environments, such as the Wadden Sea, in full
2 coverage and with high resolution and high accuracy.

3 4 **6 Conclusions**

5 A new method was developed for processing raw topobathymetric LiDAR data into a
6 digital elevation model with seamless coverage across the land-water transition zone.
7 Specifically a procedure was developed for water surface detection utilizing automatic
8 water level determination from only green LiDAR data in a tidal environment. The
9 method relies on basic principles, and in general the entire processing method is
10 described with a high level of detail, which makes it easy to implement for future
11 studies. The water surface detection method presented in this work did not take into
12 account the variation in wave heights and surface slopes, which therefore constitutes a
13 challenge to be addressed in future studies.

14 The vertical accuracy of the LiDAR data was determined by object detection of a
15 cement block on land to ± 8.1 cm with a 95% confidence level. The vertical precision
16 was determined at the cement block to ± 7.6 cm, and ± 3.8 cm at a steel frame, placed
17 just below the water surface. The horizontal mean error was determined at the block to
18 ± 10.4 cm. Overall, vertical and horizontal precision is within sub decimetre scale.

19 A seamless topobathymetric digital elevation model was created in a 4×0.85 km section
20 in the Knudedyb tidal inlet system. An average point density of 20 points per m^2 made it
21 possible to create an elevation model of 0.5×0.5 m resolution without significant
22 interpolation. The model extends down to water depths of 3 m, which was the maximum
23 penetration depth of the laser scanning system at the given environmental conditions.
24 Measurements of suspended sediment concentration and organic matter content indicate
25 that the penetration depth is limited by the amount of organic matter rather than the
26 amount of suspended sediment.

27 The vertical “dead zone” of the LiDAR data has been determined to be approx. 0-28 cm
28 in the very shallow water.

29 A morphological classification method was developed for classifying the area into 6
30 morphological classes: swash bars, linear bars, beach dunes, intertidal flats, intertidal

1 creeks and subtidal channels. The morphological classification method is based on
2 parameters of tidal range, terrain slope, a combination of various statistical
3 neighbourhood analyses with varying window sizes and the area/perimeter-ratio of
4 morphological features. The concept can be applied in any coastal environment with
5 knowledge of the tidal range and the input of a digital elevation model; however, the
6 thresholds may need adaptation, since they have been determined for the given study
7 area. In the future the classification method should be improved by implementing an
8 objective method for determining thresholds, which makes it immediately applicable
9 across different environments.

10 Overall this study has demonstrated that airborne topobathymetric LiDAR is capable of
11 seamless mapping across land-water transition zones even in environmentally
12 challenging coastal environments with high water column turbidity and continuously
13 varying water levels due to tides. Furthermore, we have demonstrated the potential of
14 topobathymetric LiDAR in combination with morphometric analyses for classification
15 of morphological features present in coastal land-water transition zones.

16 **Acknowledgements**

17 This work was funded by the Danish Council for Independent Research | Natural
18 Sciences through the project “Process-based understanding and prediction of
19 morphodynamics in a natural coastal system in response to climate change” (Steno
20 Grant no. 10-081102) and by the Geocenter Denmark through the project “Closing the
21 gap! – Coherent land-water environmental mapping (LAWA)” (Grant no. 4-2015).

22

1 **References**

- 2 Al-Hamdani, Z. K., Reker, J., Leth, J. O., Reijonen, A., Kotilainen, A. T., and Dinesen, G. E.:
3 Development of marine landscape maps for the Baltic Sea and the Kattegat using
4 geophysical and hydrographical parameters, Geological Survey of Denmark and Greenland
5 Bulletin, 13, 61-64, 2007.
- 6 Alexander, C.: Classification of Full-waveform Airborne Laser Scanning Data and
7 Extraction of Attributes of Vegetation for Topographic Mapping, PhD Thesis, University of
8 Leicester, 2010.
- 9 Allouis, T., Bailly, J. S., Pastol, Y., and Le Roux, C.: Comparison of LiDAR waveform
10 processing methods for very shallow water bathymetry using Raman, near-infrared and
11 green signals, Earth Surface Processes and Landforms, 35, 640-650, 2010.
- 12 Anderson, J. T., Van Holliday, D., Kloser, R., Reid, D. G., and Simard, Y.: Acoustic seabed
13 classification: current practice and future directions, ICES Journal of Marine Science:
14 Journal du Conseil, 65, 1004-1011, 2008.
- 15 Baltsavias, E. P.: Airborne laser scanning: basic relations and formulas, ISPRS Journal of
16 Photogrammetry and Remote Sensing, 54, 199-214, 1999.
- 17 Bradbury, J.: A keyed classification of natural geodiversity for land management and
18 nature conservation purposes, Proceedings of the Geologists' Association, 125, 329-349,
19 <http://dx.doi.org/10.1016/j.pgeola.2014.03.006>, 2014.
- 20 Brzank, A., Heipke, C., Goepfert, J., and Soergel, U.: Aspects of generating precise digital
21 terrain models in the Wadden Sea from lidar-water classification and structure line
22 extraction, ISPRS Journal of Photogrammetry and Remote Sensing, 63, 510-528, 2008.
- 23 Carr-Betts, E., Beck, T. M., and Kraus, N. C.: Tidal Inlet Morphology Classification and
24 Empirical Determination of Seaward and Down-Drift Extents of Tidal Inlets, Journal of
25 Coastal Research, 28, 547-556, 10.2307/41508568, 2012.
- 26 Chauve, A., Mallet, C., Bretar, F., Durrieu, S., Deseilligny, M. P., and Puech, W.: Processing
27 Full-Waveform LiDAR data: Modelling raw signals, Internatinal archives of
28 Photogrammetry, Remote Sensing and Spatial Information Sciences, 2007.
- 29 Collin, A., Archambault, P., and Long, B.: Mapping the shallow water seabed habitat with
30 the SHOALS, Geoscience and Remote Sensing, IEEE Transactions on, 46, 2947-2955, 2008.
- 31 Collin, A., Long, B., and Archambault, P.: Merging land-marine realms: Spatial patterns of
32 seamless coastal habitats using a multispectral LiDAR, Remote Sensing of Environment,
33 123, 390-399, 2012.
- 34 DCA (Danish Coastal Authority): Wave data - Fanø Bugt,
35 [http://kysterne.kyst.dk/pages/10852/waves/showData.asp?targetDay=30-05-](http://kysterne.kyst.dk/pages/10852/waves/showData.asp?targetDay=30-05-2014&ident=3071&subGroupGuid=16406)
36 [2014&ident=3071&subGroupGuid=16406](http://kysterne.kyst.dk/pages/10852/waves/showData.asp?targetDay=30-05-2014&ident=3071&subGroupGuid=16406), last access: 9 March 2016, 2014.
- 37 De Swart, H., and Zimmerman, J.: Morphodynamics of tidal inlet systems, Annual Review of
38 Fluid Mechanics, 41, 203-229, 2009.
- 39 Diesing, M., Coggan, R., and Vanstaen, K.: Widespread rocky reef occurrence in the central
40 English Channel and the implications for predictive habitat mapping, Estuarine, Coastal
41 and Shelf Science, 83, 647-658, 2009.
- 42 Dix, M., Abd-Elrahman, A., Dewitt, B., and Nash, L.: Accuracy Evaluation of Terrestrial
43 LIDAR and Multibeam Sonar Systems Mounted on a Survey Vessel, Journal of Surveying
44 Engineering, 138, 203-213, 10.1061/(ASCE)SU.1943-5428.0000075, 2012.

- 1 DMI (Danish Meteorological Institute): Vejr- og klimadata, Danmark - Ugeoversigt 2014 -
2 22, 26 Maj 2014 - 1 Juni 2014,
3 http://www.dmi.dk/uploads/tx_dmidatastore/webservice/t/g/i/s/r/20140601ugeoversigt.pdf,
4 last access: 9 March 2016, 2014.
- 5 Doneus, M., Doneus, N., Briese, C., Pregesbauer, M., Mandlbürger, G., and Verhoeven, G.:
6 Airborne laser bathymetry—detecting and recording submerged archaeological sites from
7 the air, *J Archeol Sci*, 40, 2136-2151, 2013.
- 8 Ernstsen, V. B., Noormets, R., Hebbeln, D., Bartholomä, A., and Flemming, B. W.: Precision
9 of high-resolution multibeam echo sounding coupled with high-accuracy positioning in a
10 shallow water coastal environment, *Geo-mar lett*, 26, 141-149, 2006a.
- 11 Ernstsen, V. B., Noormets, R., Winter, C., Hebbeln, D., Bartholomä, A., Flemming, B. W., and
12 Bartholdy, J.: Quantification of dune dynamics during a tidal cycle in an inlet channel of the
13 Danish Wadden Sea, *Geo-Marine Letters*, 26, 151-163, 2006b.
- 14 Finkl, C. W., Benedet, L., and Andrews, J. L.: Interpretation of seabed geomorphology based
15 on spatial analysis of high-density airborne laser bathymetry, *Journal of Coastal Research*,
16 501-514, 2005.
- 17 FitzGerald, D., Buynevich, I., and Hein, C.: Morphodynamics and facies architecture of tidal
18 inlets and tidal deltas, in: *Principles of Tidal Sedimentology*, Springer, 301-333, 2012.
- 19 Graham, L.: Accuracy. Precision and all That Jazz, *LiDAR Magazine*, 2, 2012.
- 20 Guenther, G. C.: Airborne laser hydrography: System design and performance factors, DTIC
21 Document, 1985.
- 22 Guenther, G. C., Cunningham, A. G., LaRocque, P. E., and Reid, D. J.: Meeting the accuracy
23 challenge in airborne lidar bathymetry, *EARSel*, Dresden, 2000.
- 24 Guenther, G. C.: Airborne lidar bathymetry, *Digital elevation model technologies and
25 applications: The DEM users manual*, 2, 253-320, 2007.
- 26 Hladik, C., and Alber, M.: Accuracy assessment and correction of a LIDAR-derived salt
27 marsh digital elevation model, *Remote Sens Environ*, 121, 224-235, 2012.
- 28 Hofle, B., Vetter, M., Pfeifer, N., Mandlbürger, G., and Stotter, J.: Water surface mapping
29 from airborne laser scanning using signal intensity and elevation data, *Earth Surface
30 Processes and Landforms*, 34, 1635, 2009.
- 31 Huising, E. J., and Gomes Pereira, L. M.: Errors and accuracy estimates of laser data
32 acquired by various laser scanning systems for topographic applications, *ISPRS Journal of
33 Photogrammetry and Remote Sensing*, 53, 245-261, [http://dx.doi.org/10.1016/S0924-
34 2716\(98\)00013-6](http://dx.doi.org/10.1016/S0924-2716(98)00013-6), 1998.
- 35 IHO: IHO Standards for Hydrographic Surveys (S-44), 5th edition, International
36 Hydrographic Bureau Monaco, 2008.
- 37 Ismail, K., Huvenne, V. A., and Masson, D. G.: Objective automated classification technique
38 for marine landscape mapping in submarine canyons, *Marine Geology*, 362, 17-32, 2015.
- 39 Jensen, J. R.: *Remote sensing of the environment: An earth resource perspective 2/e*,
40 Pearson Education India, 2009.
- 41 Kaskela, A. M., Kotilainen, A. T., Al-Hamdani, Z., Leth, J. O., and Reker, J.: Seabed geomorphic
42 features in a glaciated shelf of the Baltic Sea, *Estuarine, Coastal and Shelf Science*, 100,
43 150-161, <http://dx.doi.org/10.1016/j.ecss.2012.01.008>, 2012.

- 1 Klagenberg, P. A., Knudsen, S. B., Sørensen, C., and Sørensen, P.: Morfologisk udvikling i
2 Vadehavet: Knudedybs tidevandsområde, Kystdirektoratet, 2008.
- 3 Klemas, V.: Airborne remote sensing of coastal features and processes: An overview, J
4 Coastal Res, 29, 239-255, 2013.
- 5 Kunz, G., Lamberts, C., van Mierlo, G., de Vries, F., Visser, H., Smorenburg, C., Spitzer, D., and
6 Hofstraat, H.: Laser bathymetry in the Netherlands, EAR-SeL Advances in Remote Sensing,
7 36-41, 1992.
- 8 Lefebvre, A., Ernstsens, V. B., and Winter, C.: Estimation of roughness lengths and flow
9 separation over compound bedforms in a natural-tidal inlet, Cont Shelf Res, 61-62, 98-111,
10 10.1016/j.csr.2013.04.030, 2013.
- 11 Leica: Leica LiDAR Survey Studio flyer, available at: [http://leica-
12 geosystems.com/products/airborne-systems/software/leica-lidar-survey-studio](http://leica-geosystems.com/products/airborne-systems/software/leica-lidar-survey-studio), last
13 access: 24 March 2016, Heerbrugg, Switzerland, 2015.
- 14 Lundblad, E. R., Wright, D. J., Miller, J., Larkin, E. M., Rinehart, R., Naar, D. F., Donahue, B. T.,
15 Anderson, S. M., and Battista, T.: A benthic terrain classification scheme for American
16 Samoa, Marine Geodesy, 29, 89-111, 2006.
- 17 Mallet, C., and Bretar, F.: Full-waveform topographic lidar: State-of-the-art, ISPRS J
18 Photogramm, 64, 1-16, 2009.
- 19 Mandlbürger, G., Pfennigbauer, M., Steinbacher, F., and Pfeifer, N.: Airborne Hydrographic
20 LiDAR Mapping-Potential of a new technique for capturing shallow water bodies,
21 Proceedings of ModSim'11, 2011.
- 22 Mandlbürger, G., Pfennigbauer, M., and Pfeifer, N.: Analyzing near water surface
23 penetration in laser bathymetry-A case study at the River Pielach, ISPRS Annals of
24 Photogrammetry, Remote Sensing and Spatial Information Sciences, 1, 175-180, 2013.
- 25 Mandlbürger, G., Hauer, C., Wieser, M., and Pfeifer, N.: Topo-bathymetric LiDAR for
26 monitoring river morphodynamics and instream habitats—A case study at the Pielach
27 River, Remote Sensing, 7, 6160-6195, 2015.
- 28 Millard, R. C., and Seaver, G.: An index of refraction algorithm for seawater over
29 temperature, pressure, salinity, density, and wavelength, Deep Sea Research Part A.
30 Oceanographic Research Papers, 37, 1909-1926, [http://dx.doi.org/10.1016/
31 0149\(90\)90086-B](http://dx.doi.org/10.1016/0198-0149(90)90086-B), 1990.
- 32 Mousavi, M., Irish, J., Frey, A., Olivera, F., and Edge, B.: Global warming and hurricanes: the
33 potential impact of hurricane intensification and sea level rise on coastal flooding, Climatic
34 Change, 104, 575-597, 10.1007/s10584-009-9790-0, 2011.
- 35 Nayegandhi, A., Brock, J., and Wright, C.: Small-footprint, waveform-resolving lidar
36 estimation of submerged and sub-canopy topography in coastal environments, Int J
37 Remote Sens, 30, 861-878, 2009.
- 38 Niemeyer, J., and Soergel, U.: Opportunities of Airborne Laser Bathymetry for the
39 Monitoring of the Sea Bed on the Baltic Sea Coast, ISPRS J Photogramm, Remote Sensing
40 and Spatial Information Sciences, 1, 179-184, 2013.
- 41 Optech: Optech HydroFusion Information Sheet, available at:
42 http://www.teledyneoptech.com/wp-content/uploads/specification_hydrofusion.pdf, last
43 access: 24 March 2016, Canada, 2013.
- 44 Parker, H., and Sinclair, M.: The successful application of Airborne LiDAR Bathymetry
45 surveys using latest technology, OCEANS, 2012 - Yeosu, 2012, 1-4,

- 1 Pastol, Y., Le Roux, C., and Louvart, L.: LITTO D-A Seamless Digital Terrain Model, The
2 International hydrographic review, 8, 2007.
- 3 Pe'eri, S., and Long, B.: LIDAR technology applied in coastal studies and management, J
4 Coastal Res, 1-5, 2011.
- 5 Pedersen, J. B. T., and Bartholdy, J.: Budgets for fine-grained sediment in the Danish
6 Wadden Sea, Mar Geol, 235, 101-117, 2006.
- 7 RIEGL: LAS extrabytes implementation in RIEGL software - Whitepaper, RIEGL Laser
8 Measurement Systems GmbH, available at:
9 [www.riegl.com/uploads/tx_pxpriegldownloads/Whitepaper -
10 _LAS extrabytes implementation in Riegl software 01.pdf](http://www.riegl.com/uploads/tx_pxpriegldownloads/Whitepaper_-_LAS_extrabytes_implementation_in_Riegl_software_01.pdf), last access: 24 March 2016,
11 2012.
- 12 RIEGL: Datasheet RIEGL VQ-820-G, RIEGL Laser Measurement Systems GmbH, available
13 at: [http://www.riegl.com/uploads/tx_pxpriegldownloads/DataSheet_VQ-820-G_2015-03-
14 24.pdf](http://www.riegl.com/uploads/tx_pxpriegldownloads/DataSheet_VQ-820-G_2015-03-24.pdf), last access: 24 March 2016, 2014.
- 15 RIEGL: Data Sheet RiHYDRO, RIEGL Laser Measurement Systems GmbH, available at:
16 [http://www.riegl.com/uploads/tx_pxpriegldownloads/11_DataSheet_RiHYDRO_2015-08-
17 24_01.pdf](http://www.riegl.com/uploads/tx_pxpriegldownloads/11_DataSheet_RiHYDRO_2015-08-24_01.pdf), last access: 24 March 2016, 2015.
- 18 Rinehart, R., Wright, D. J., Lundblad, E. R., Larkin, E. M., Murphy, J., and Cary-Kothera, L.:
19 ArcGIS 8. x benthic terrain modeler: Analysis in American Samoa, Proceedings of the 24th
20 Annual ESRI User Conference, San Diego, CA, Paper, 2004, 2004,
- 21 Sacchetti, F., Benetti, S., Georgiopoulou, A., Dunlop, P., and Quinn, R.: Geomorphology of the
22 Irish Rockall Trough, North Atlantic Ocean, mapped from multibeam bathymetric and
23 backscatter data, Journal of Maps, 7, 60-81, 2011.
- 24 Schmidt, A., Rottensteiner, F., and Soergel, U.: Classification of airborne laser scanning data
25 in Wadden sea areas using conditional random fields, International Archives of the
26 Photogrammetry, Remote Sensing and Spatial Information Sciences XXIX-B3, 161-166,
27 2012.
- 28 Steinbacher, F., Pfennigbauer, M., Aufleger, M., and Ullrich, A.: High resolution airborne
29 shallow water mapping, International Archives of the Photogrammetry, Remote Sensing
30 and Spatial Information Sciences, Proceedings of the XXII ISPRS Congress, 2012,
- 31 Su, L., and Gibeaut, J.: EXTRACTING SURFACE FEATURES OF THE NUECES RIVER DELTA
32 USING LIDAR POINTS, ASPRS/MAPPS 2009 Fall Conference, San Antonio, Texas,
33 November 16-19, 2009.
- 34 Verfaillie, E., Doornenbal, P., Mitchell, A. J., White, J., and Van Lancker, V.: The bathymetric
35 position index (BPI) as a support tool for habitat mapping. Worked example for the MESH
36 Final Guidance, 14 pp., 2007.
- 37 Wang, C.-K., and Philpot, W. D.: Using airborne bathymetric lidar to detect bottom type
38 variation in shallow waters, Remote Sensing of Environment, 106, 123-135, 2007.
- 39 Wright, D., Lundblad, E., Larkin, E., Rinehart, R., Murphy, J., Cary-Kothera, L., and Draganov,
40 K.: ArcGIS Benthic Terrain Modeler, Corvallis, Oregon, Oregon State University, Davey
41 Jones Locker Seafloor Mapping/Marine GIS Laboratory and NOAA Coastal Services Center,
42 Accessible online at: <http://www.csc.noaa.gov/products/btm>, 2005.
- 43
- 44

1

2 Table 1: Vertical accuracy and precision of the LiDAR point measurements, in terms of
 3 minimum error (E_{\min}), maximum error (E_{\max}), standard deviation (σ), mean absolute
 4 error (E_{MA}), root mean square error (E_{RMS}) and the 95% confidence level ($Cl_{95\%}$).

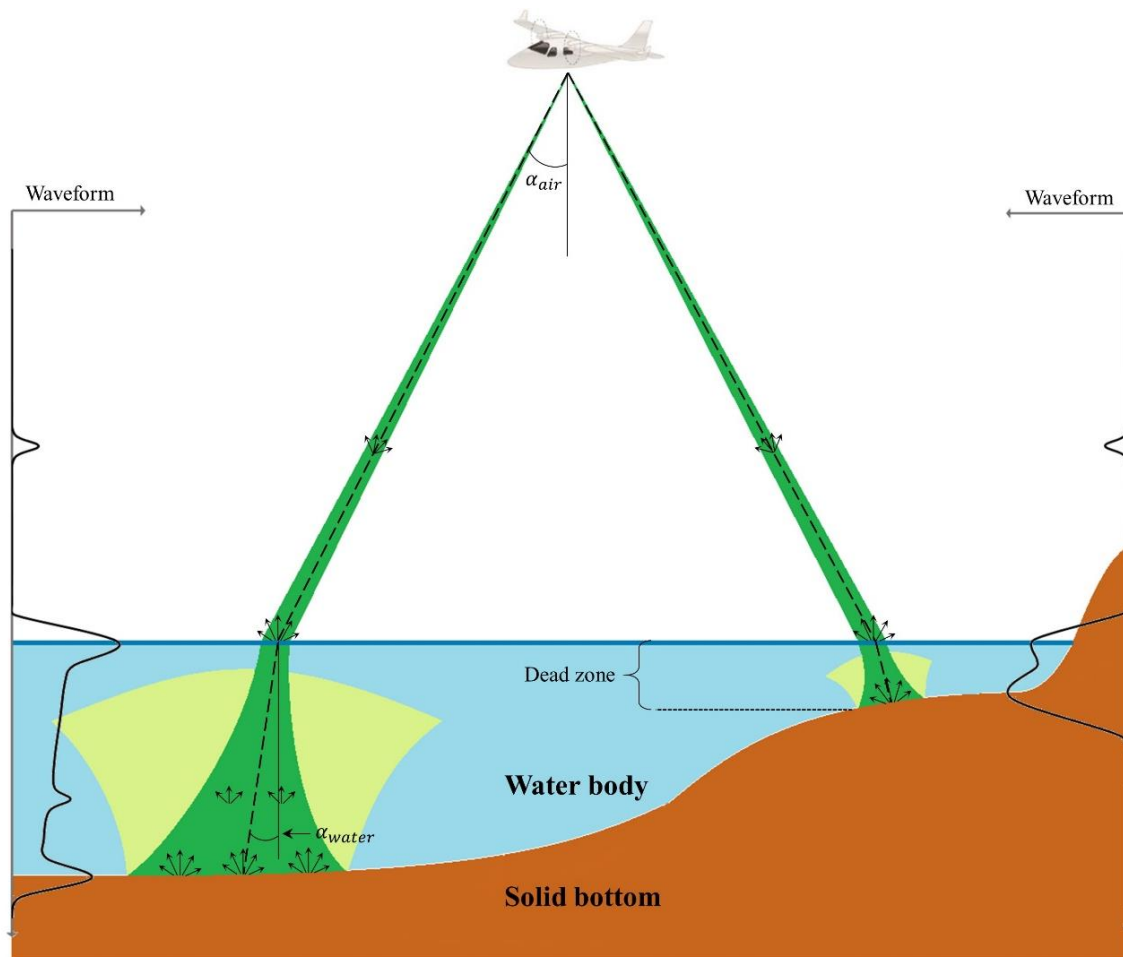
Accuracy/ Precision	Object	Best-fit plane	# points n	E_{\min} (cm)	E_{\max} (cm)	σ (cm)	E_{MA} (cm)	E_{RMS} (cm)	$Cl_{95\%}$ (cm)
Accuracy	Cement block	GCPs	227	0.01	12.1	4.1	3.5	± 4.1	± 8.1
Precision	Cement block	Point cloud	227	0.04	12.9	3.9	2.8	± 3.9	± 7.6
Precision	Steel frame	Point cloud	46	0.02	5.5	2.0	1.6	± 1.9	± 3.8

5

1 Table 2: LiDAR point spacing and density for all the 11 individual swaths, which
 2 covered the study area, and for the combined swaths.

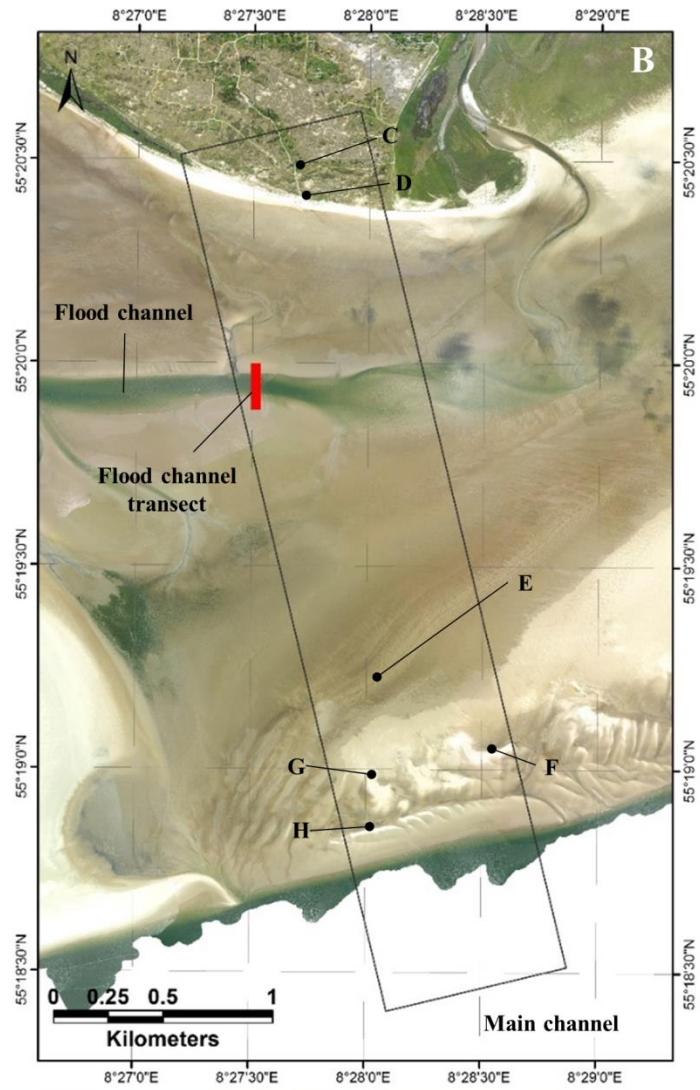
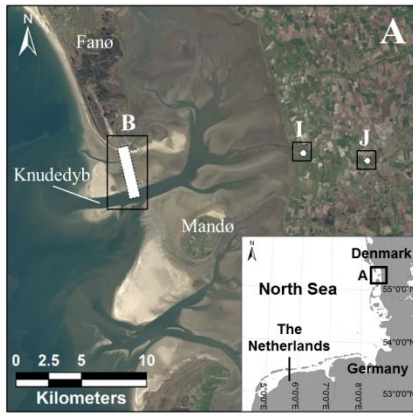
Swath number	1	2	3	4	5	6	7	8	9	10	11	All
Point spacing (m)	0.30	0.30	0.36	0.31	0.36	0.32	0.37	0.29	0.35	0.36	0.28	0.20
Point density (pt./m ²)	10.8	10.8	7.8	10.2	7.5	9.6	7.2	11.7	8.0	7.8	12.7	19.6

3



1

2 Figure 1: Conceptual sketch of the laser beam propagation and return signals. The beam
 3 refracts upon entering the water body, and it diverges as it propagates through the water
 4 column. Return signals are produced both in the air, at the water surface, in the water
 5 column and at the seabed. The LiDAR instrument has limited capability in very shallow
 6 water (the “dead zone” in the figure) because the successive peaks from the water
 7 surface and the seabed are not individually separated in time and amplitude. Only the
 8 largest peak, which is from the seabed, is detected.



1

1 Figure 2: A) Overview of the study area location in the Danish Wadden Sea and the
2 specific locations of the study site (B) and the two validation sites (I and J) (22 April
3 2015 satellite image, Landsat 8). B) The study site in the Knudedyb tidal inlet system
4 (30 May 2015 Orthophoto, AHM). C) Cottages in the dunes on Fanø. D) Beach dunes
5 on Fanø. E) Patch of *Spartina Townsendii* (Common Cord Grass). F-G) Swash bars. H)
6 Linear bar. I) Validation site 1 with a cement block on land, used for accuracy and
7 precision assessment (19 April 2015 orthophoto, AHM). J) Validation site 2 with a steel
8 frame in Ribe Vesterå River, used for precision assessment (19 April 2015 orthophoto,
9 AHM).

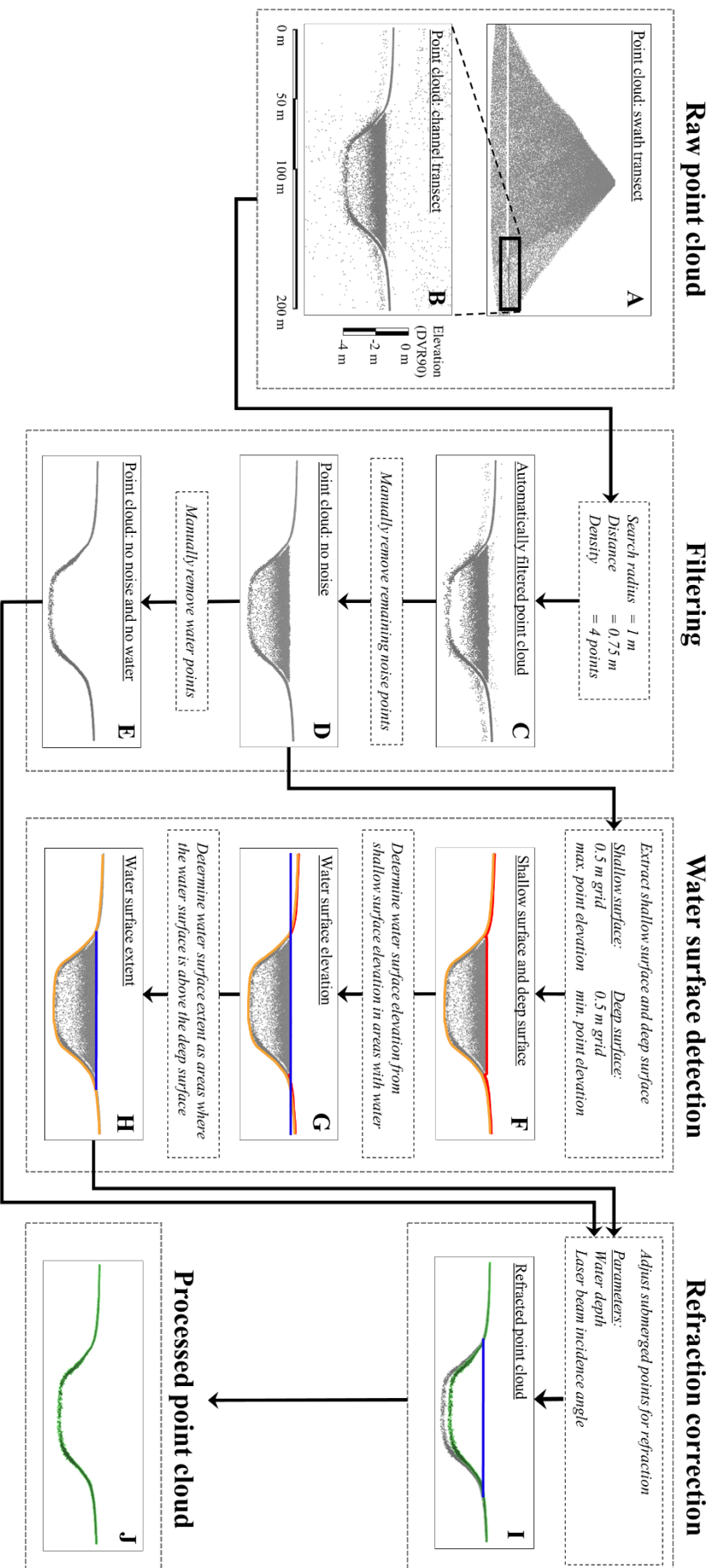
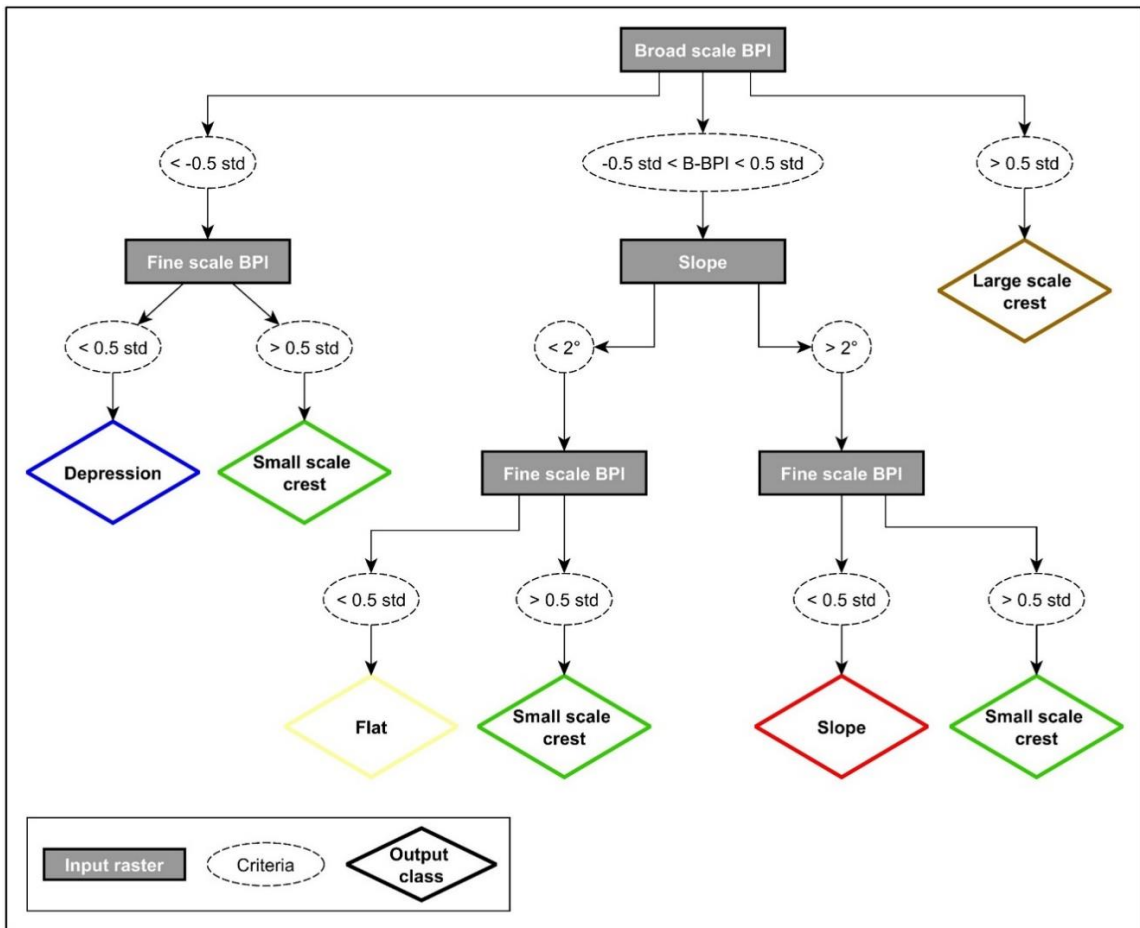


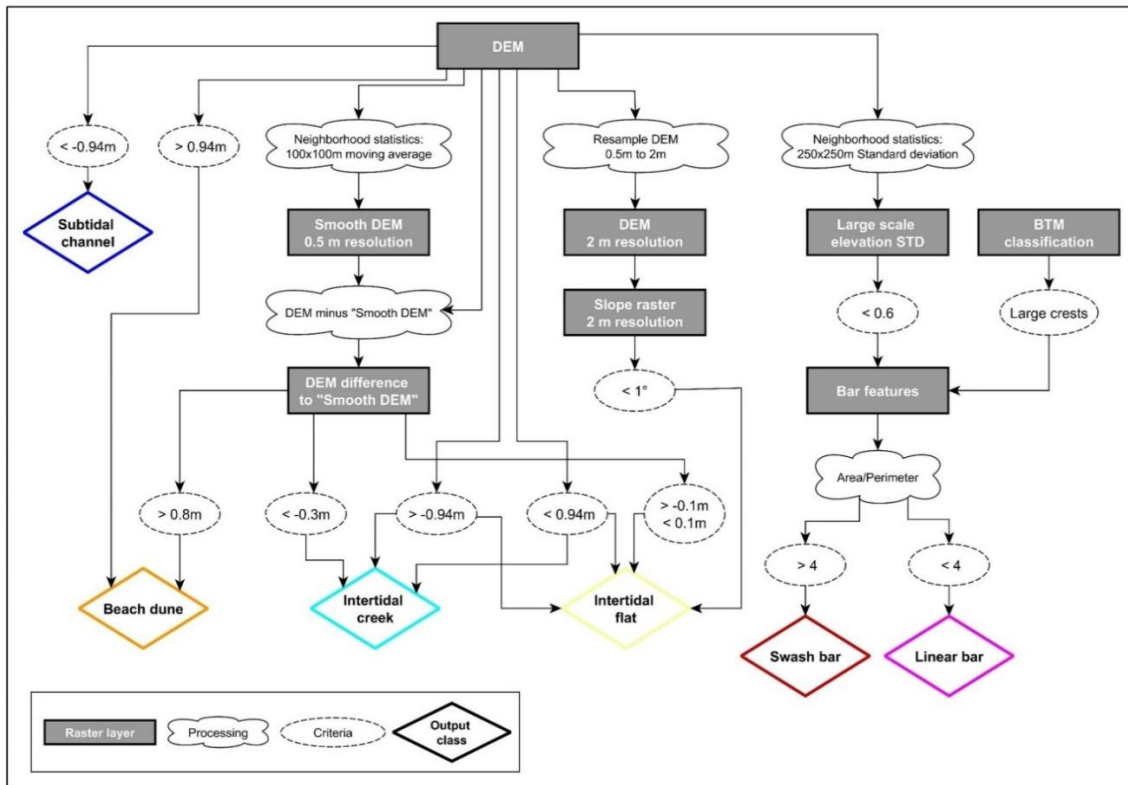
Figure 3: Workflow for processing the LIDAR point cloud. A) Point cloud from a single swath with points ranging from -100 m to 300 m elevation. B) Zoom-in on a cross section of the flood channel with altitudes exaggerated $\times 15$ for visualization purpose. C-E) Method for filtering the point cloud. F-H) Method for detecting a water surface (blue) based on the extraction of a shallow surface (red) and a deep surface (orange). I) Correction for the effect of refraction on all the submerged points. J) Processed point cloud



1

2 Figure 4: Classification decision tree, showing how the geomorphometric classification
 3 was conducted in the Benthic Terrain Model tool.

4

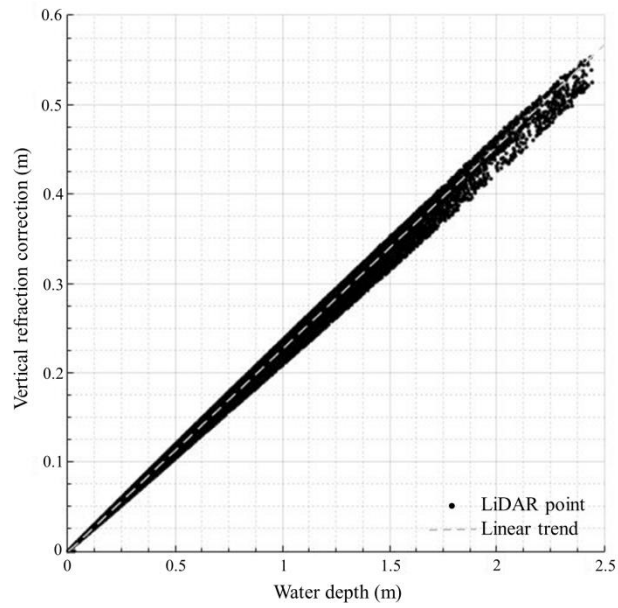


1

2 Figure 5: Classification decision tree of the morphological classification. All steps were
 3 performed in ArcGIS.

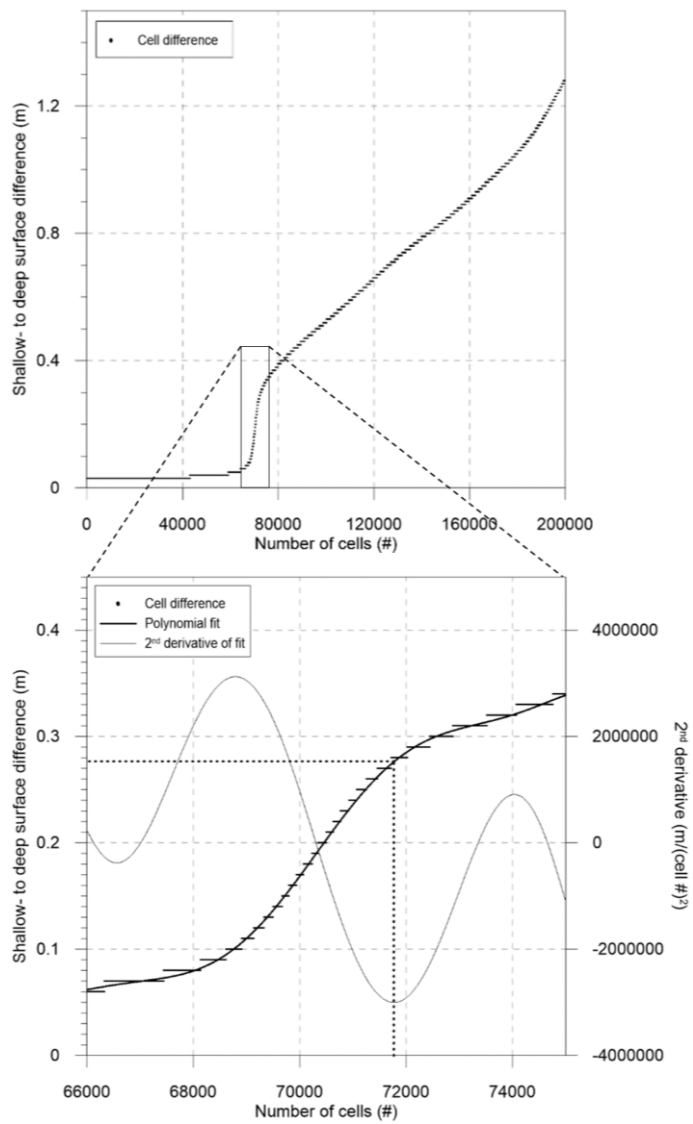
4

1



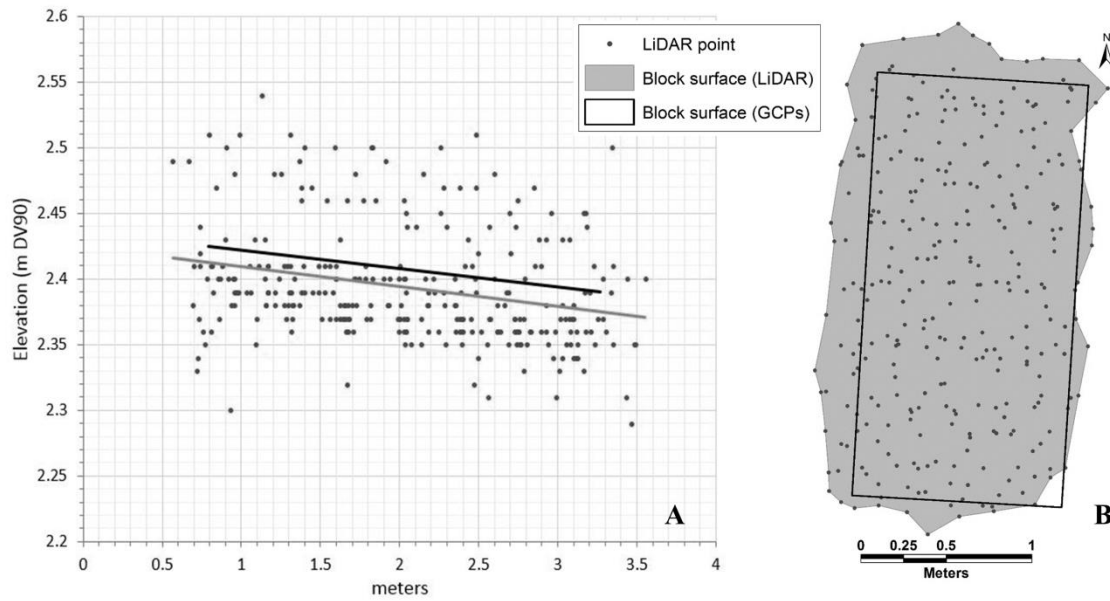
2

3 Figure 6: Vertical adjustment of the refracted LiDAR points from the flood channel
4 transect (see location in Fig. 2C).



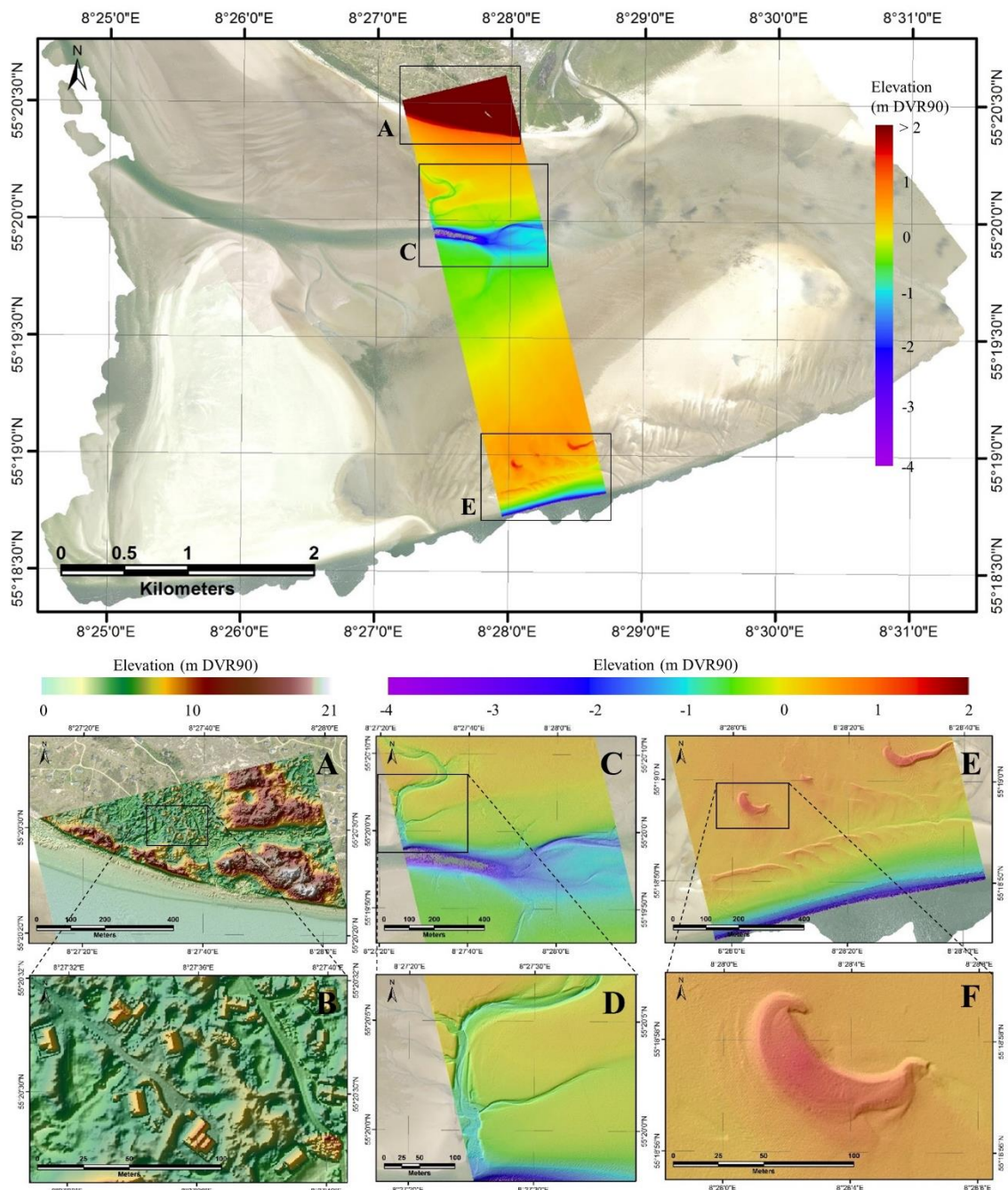
1

2 Figure 7: Vertical difference between the shallowest and the deepest LiDAR point
 3 within 0.5 m grid cells in the land-water transition zone. The abrupt change is caused
 4 by the dead zone. The vertical extent of the dead zone is determined to approx. 28 cm,
 5 derived by the maximum rate of change of a polynomial fit through the points.



1

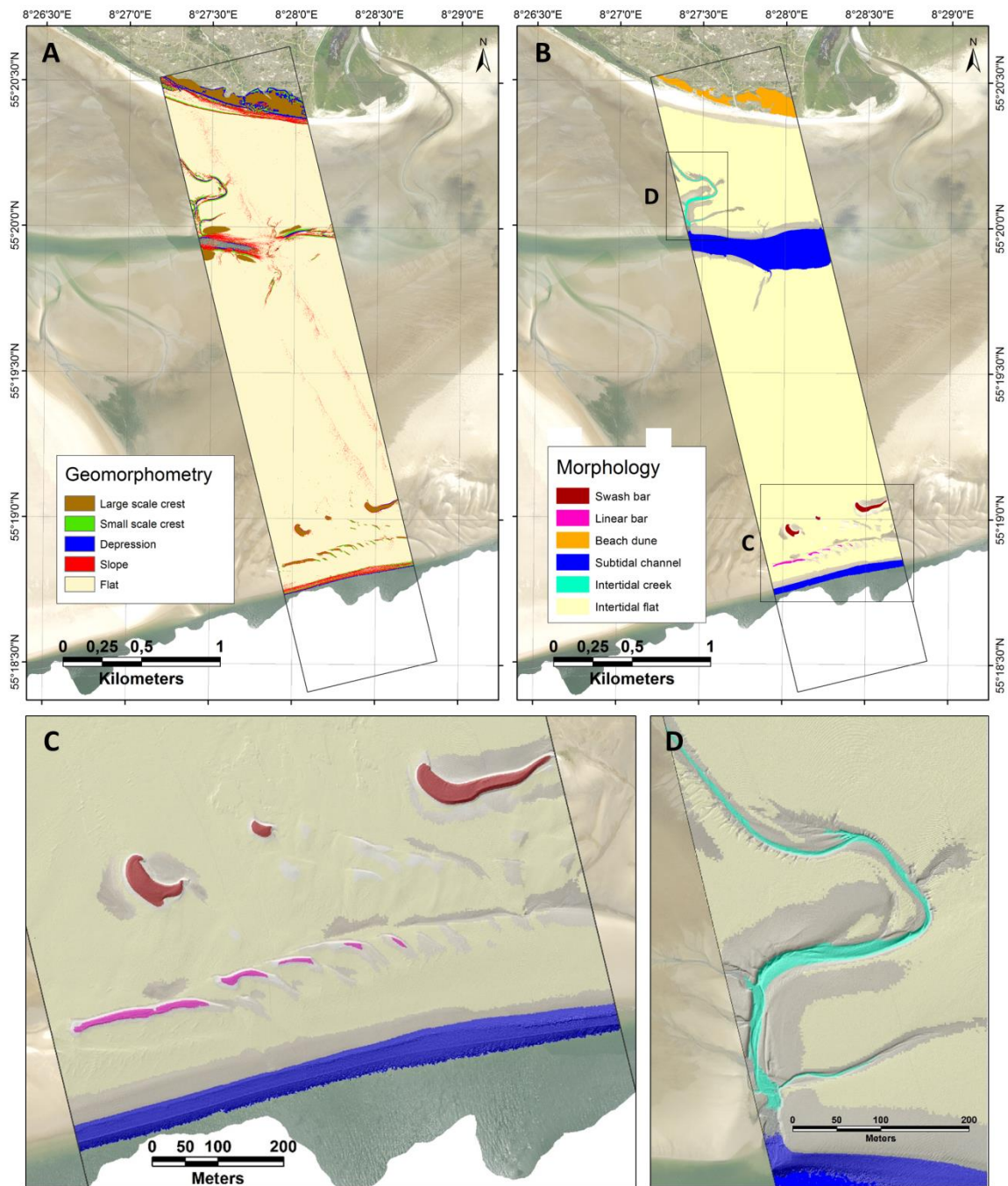
2 Figure 8: Vertical and horizontal distribution of the LiDAR points describing the block
 3 surface and the block surface derived from Ground Control Points (GCPs). A) LiDAR
 4 points (grey dots) compared to the GCP block surface (black line) for determining the
 5 vertical accuracy. The grey line shows the LiDAR block surface as a best-linear-fit
 6 through the points. B) Block surface derived from the four GCP corner points and the
 7 block surface derived by the perimeter of the LiDAR points.



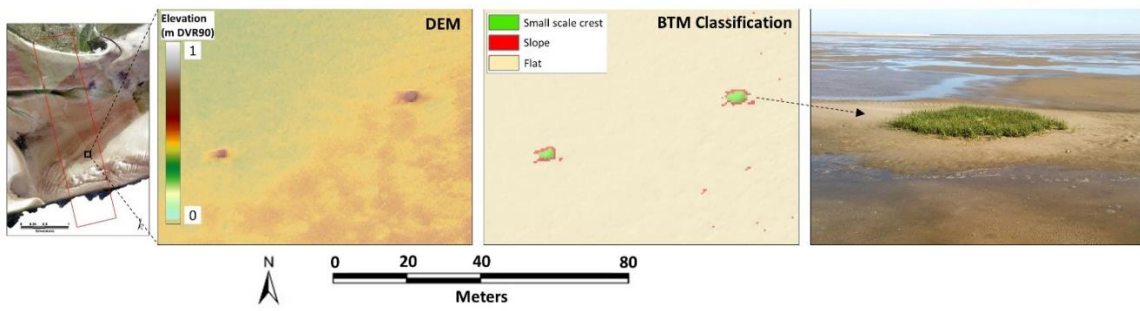
1

2 Figure 9: Topobathymetric DEM across the northern part of the Knudedyb tidal inlet
 3 system with close-up views of different detail level on specific areas. A hill shade is
 4 draped upon the close-ups for improved visualization of morphological features. A)
 5 Northern section with beach dunes and cottages. B) Cottages. C) Mid-section with the
 6 flood channel. D) Closer view on an intertidal creek. E) Southern section with swash
 7 bars, linear bars and bathymetry of the main channel. F) Swash bar.

8

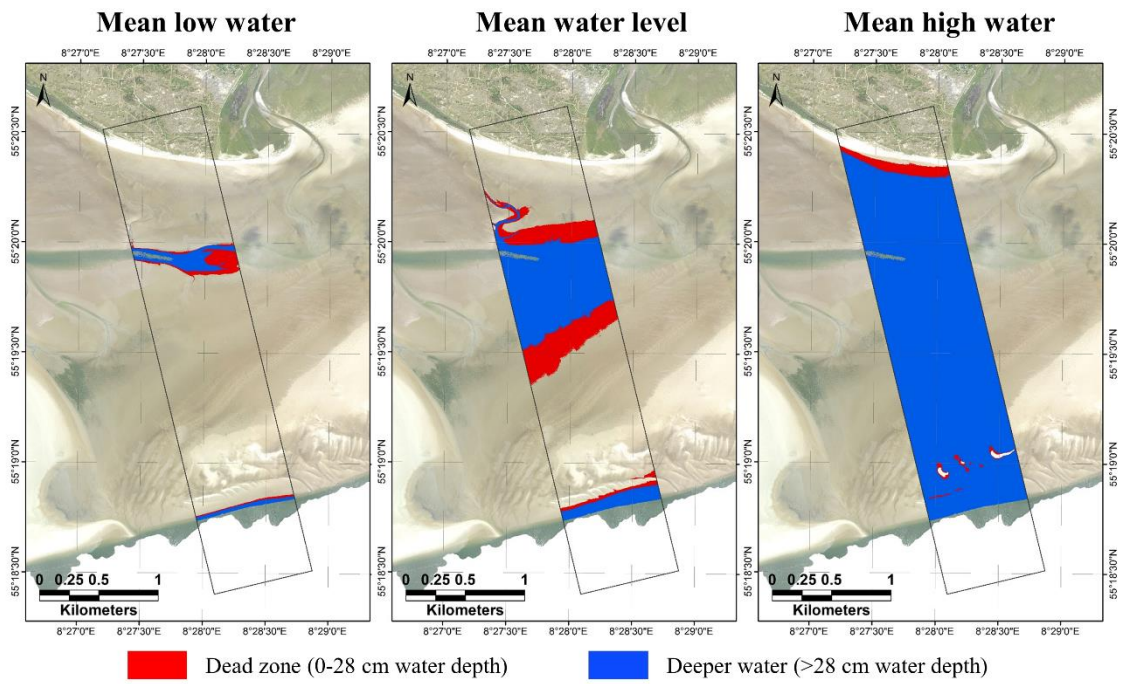


1
 2 Figure 10: Two classifications of the investigated section in Knudedyb tidal inlet
 3 system, derived from a topobathymetric DEM. A) Geomorphometric classification. B)
 4 morphological classification. C) Zoom-in on the intertidal creek in the morphological
 5 classification. D) Zoom-in on the swash bars and linear bars close to the main channel
 6 in the morphological classification. A hillshade of the DEM is draped over C and D.

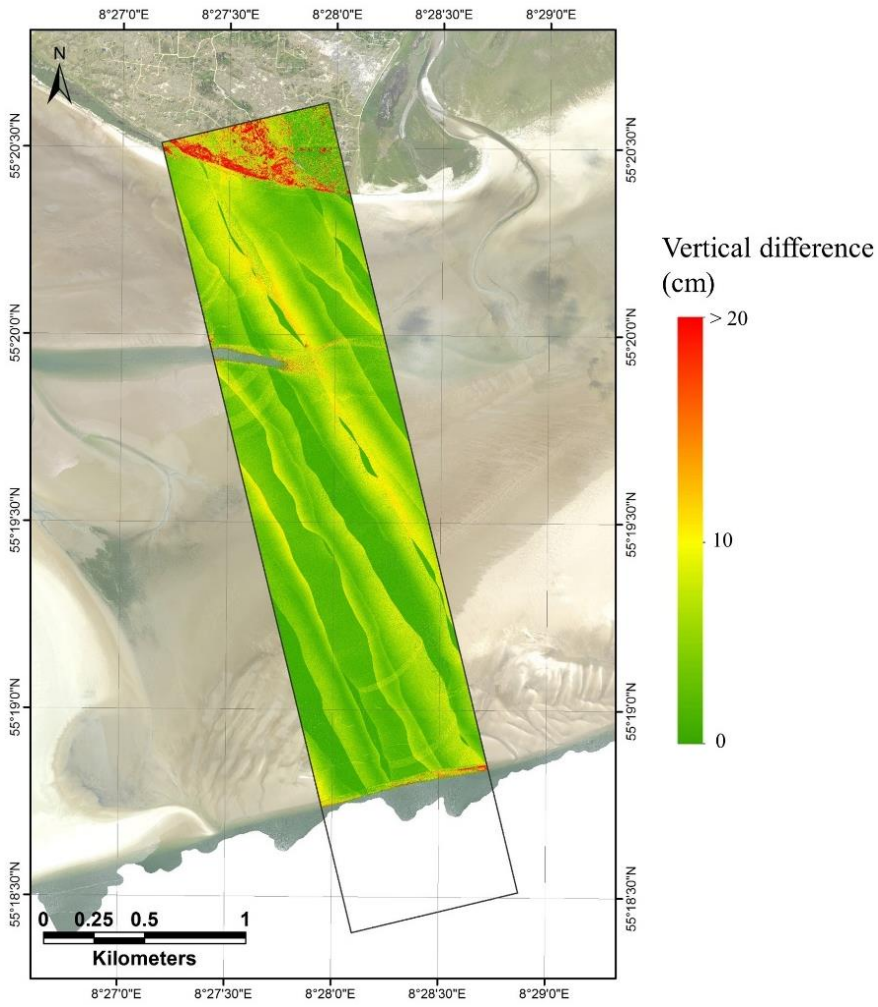


1
2
3
4
5

Figure 11: Vegetated mounds on the intertidal flat are clearly visible in the DEM and classified as small-scale crests in the geomorphometric BTM classification. To the right is an image of one of the patches.



- 1
- 2 Figure 12: Horizontal extent of the dead zone in the studied area at mean low water,
- 3 mean water level and mean high water.



1

2 Figure 13: Vertical difference between the highest and the lowest LiDAR point within
 3 0.5×0.5 m grid cells.